
Since January 2020 Elsevier has created a COVID-19 resource centre with free information in English and Mandarin on the novel coronavirus COVID-19. The COVID-19 resource centre is hosted on Elsevier Connect, the company's public news and information website.

Journal of Molecular Structure 1270 (2022) 134005

Contents lists available at ScienceDirect

Journal of Molecular Structure

journal homepage: www.elsevier.com/locate/molstr

# Synthesis, characterization, DFT, antioxidant, antibacterial, pharmacokinetics and inhibition of SARS-CoV-2 main protease of some heterocyclic hydrazones

Lilia Adjissi[a], Nadjib Chafai[a,*], Khalissa Benbouguerra[a], Imene Kirouani[a], Abdelkader Hellal[a], Houdheifa Layaida[a], Meriem Elkolli[b], Chawki Bensouici[c], Salah Chafaa[a]

[a] Laboratory of Electrochemistry of Molecular Materials and Complex (LEMMC). Department of Process Engineering, Faculty of Technology, University of Ferhat ABBAS Setif-1, El-Mabouda campus, 19000 Sétif, Algeria
[b] Laboratory of applied microbiology, Faculty of Natural and Life Sciences, University of Setif 1, Algeria
[c] Centre de Recherche en Biotechnologie, Ali Mendjli, Nouvelle Ville UV 03, BP E73 Constantine, Algeria

ARTICLE INFO

*Article history:*
Received 20 May 2022
Revised 5 August 2022
Accepted 22 August 2022
Available online 23 August 2022

*Keywords:*
Hydrazones
Synthesis
DFT
Antioxidant
Antibacterial
SARS-CoV-2

ABSTRACT

Three hydrazone derivatives have been synthesized using condensation reaction of 4-hydrazinylbenzoic acid with three aromatic aldehydes namely: thiophene-2-carbaldehyde, thiophene-3-carbaldehyde and 2-furaldehyde in ethanol at 78 °C reflux. The synthesized molecules have been characterized using spectroscopic and physicochemical methods including UV–Vis, IR, $^{1}$H NMR, $^{13}$C NMR, $^{15}$N NMR and melting point determination. Optimized molecular structures, UV–Vis and IR spectra modeling, the reactivity, the stability and some quantum chemical parameters of the synthesized molecules were modeled utilizing density functional theory (DFT). The obtained theoretical results were found in good agreement with the experimental results. On the other hand, the antioxidant and antibacterial activities of the molecules under study were evaluated to better understand the associated mechanisms of action specifically. Also, predicted ADME-T and pharmacokinetic parameters indicated that these compounds showed good oral bioavailability. Finally, molecular docking has been used to predict the inhibitory activity of the studied hydrazone derivatives on the SARS-CoV-2 main protease (Mpro).



## 1. Introduction

Hydrazone derivatives are considered among the most important molecules in organic chemistry, which show an efficient activity in a wide range of applications including development of new drugs with anti-cancer [1–4], antimicrobial [5–7], analgesic [8], antihypertensive [9], anticonvulsant [10], anti-inflammatory [11], antituberculosis [12,13], antitumoral [14,15], anti-HIV [16,17], antimalarial [18], antidepressant [19], vasodilatory [20], anti-Alzheimer [21,22], and anti-corrosion activities [23,24]. The presence of both N−N and C=N functional groups in the structure of hydrazones is responsible of their high therapeutic activity [25].

The most common process to prepare hydrazone compounds consists in heating the appropriate hydrazines with different aldehydes or ketones in various organic solvents such as ethanol and methanol. Gudasi et al. described the ineffectiveness of synthesizing hydrazone by condensing carbaldehyde with *o*-aminobenzoylhydrazide [26–28]. Another synthesis route of hydrazones consists in coupling aryldiazonium salt with active hydrogen compound [29].

Recently, DFT (Density Functional Theory) calculations have mostly been utilized to determine the active sites of organic compounds [30–32]. Also, the electronic and structural properties calculated by DFT can be used to correlate different activities of chemical species [33–35]. DFT calculations with B3LYP/6–311++*G*(d,p) as the basis set have also been used to determine the optimized geometry, dipole moment, polarizability, $E_{HOMO}$-$E_{LUMO}$ energy, molecular electrostatic potential and excited state energy [36,37].

During the last two years, scientists have accelerated the researches to discover new drugs and vaccines to combat COVID-19 pandemic. In this context, the crystalline structure of SARS-CoV-2 main protease (Mpro) is considered as a target to discover therapeutic agents to COVID-19 [38]. Also, the molecular docking calculations are a useful pathway to predict the inhibitive activity of organic compounds towards Mpro, by studying the possible interactions and energies required to inhibit the activity of Mpro [38–41].

* Corresponding author.
*E-mail address:* n.chafai@univ-setif.dz (N. Chafai).

https://doi.org/10.1016/j.molstruc.2022.134005
0022-2860/

This work reports the synthesis and spectral analysis of three hydrazone derivatives, namely: 4-{(2*E*)−2-[(*thiophen*-2-*yl*)*methylidene*]hydrazinyl}benzoic acid (**HYDZ-1**), 4-{(2*E*)−2-[(*thiophen*-3-*yl*)*methylidene*]hydrazinyl}benzoic acid (**HYDZ-2**) and 4-{(2*E*)−2-[(*furan*-2-*yl*)*methylidene*]hydrazinyl}benzoic acid (**HYDZ-3**). The synthesized molecules have been characterized by spectroscopic and physicochemical methods such as UV–Vis, IR, $^{1}$H NMR, $^{13}$C NMR, $^{15}$N NMR and melting point. Density functional theory was used to calculate the optimized molecular structures, UV–Vis and IR spectra, the highest occupied molecular orbital (HOMO) and lowest unoccupied molecular orbital (LUMO), the reactivity, the stability, and some quantum chemical parameters of the investigated molecules. On the other hand, the biological activities of the synthesized hydrazones were evaluated. Also, the inhibition activity of SARS-CoV-2 main protease of the synthesized molecules has been evaluated *in silico* by molecular docking calculations. It is noted that is the first time that these molecules were tested.

## 2. Chemistry, materials and methods

### 2.1. Chemical reagents

All the compounds used in this work for the syntheses of the investigated hydrazones are commercially available and purchased from Sigma-Aldrich and Fluka. In addition, they were used without any further purification.

### 2.2. General procedure for the synthesis of hydrazone derivatives

#### 2.2.1. 4-{(2E)−2-[(thiophen-2-yl)methylidene]hydrazinyl}benzoic acid (HYDZ-1)

According to Fig. 1, 1.0 mmol of 4-hydrazinylbenzoic acid 97% and 1.0 mmol of thiophene-2-carbaldehyde 98% are dissolved in ethanol. The mixture was refluxed at a temperature of 78 °C for 10 h. The resulting crude solution was cooled at room temperature and kept clear until a solid precipitate forms. The resulting product was purified by methanol crystallization. The yellow solid hydrazone is produced in yield 79%. MF: $C_{12}H_{10}N_2O_2S$, M.p. 240.02 °C, UV–Vis (Methanol), $\lambda_{max}$ (nm): 363. IR (ATR, $\nu$ ($cm^{-1}$)): 3502 (O–H), 3311 (N–H), 3276 (C–$H_{Ar}$), 2930 (C–$H_{Alph}$), 1661 (C=O), 1593 (N=$C_{Ar}$), 1541 (C–H), 1273 (C–N), 1138 (N–N), 1090 (C–O), 852 (C-S), 685 (N–H). **$^{1}$H NMR** (400 MHz, DMSO, $\delta$(ppm)): 7.01 (s, 1H, -C **H**$_{Ar5}$), 7.10 (s, 1H, C **H**$_{Ar3}$), 7.30 (d, 2H, C **H**$_{Ar8-}$C **H**$_{Ar9}$), 7.55 (s, 1H, C **H**$_{Ar4}$-S), 7.83 (d, 2H, C **H**$_{Ar10-}$C **H**$_{Ar11}$), 8.15 (s, 1H, C **H**=N), 10.75 (s, 1H, -N **H** –N), 12.23 (s, 1H, O **H**) ; **$^{13}$C NMR**: (75 MHz, DMSO, $\delta$(ppm)): 111.54 (d, 2C, **C**$H_{Ar10-}$ **C**$H_{Ar11}$), 120.84 (s, 1C, **C**$_{Ar12}$), 127.13 (s, 1C, **C**$H_{Ar5}$), 128.17 (s, 1C, - **C**H=N-N-), 128.30 (s, 1C, **C**$H_{Ar4}$-S), 131.69 (d, 2C, **C**$_{Ar10-}$ **C**$_{Ar11}$), 134.93 (s, 1C, **C**$H_{Ar3}$), 140.71 (s, 1C, **C**$_{Ar1}$-S), 148.99 (s, 1C, **C**$_{Ar7-}$NH), 167.74 (s, 1C, **C**OOH) ; **$^{15}$N NMR**, DMSO, $\delta$(ppm) : 147.71 (s, 2 N, - **N**H– **N** = C).

#### 2.2.2. 4-{(2E)−2-[(thiophen-3yl)methylidene]hydrazinyl}benzoic acid (HYDZ-2)

**HYDZ-2** is prepared by dissolving 1.0 mmol of 4-hydrazinylbenzoic acid 97% and 1.0 mmol of thiophene-3-

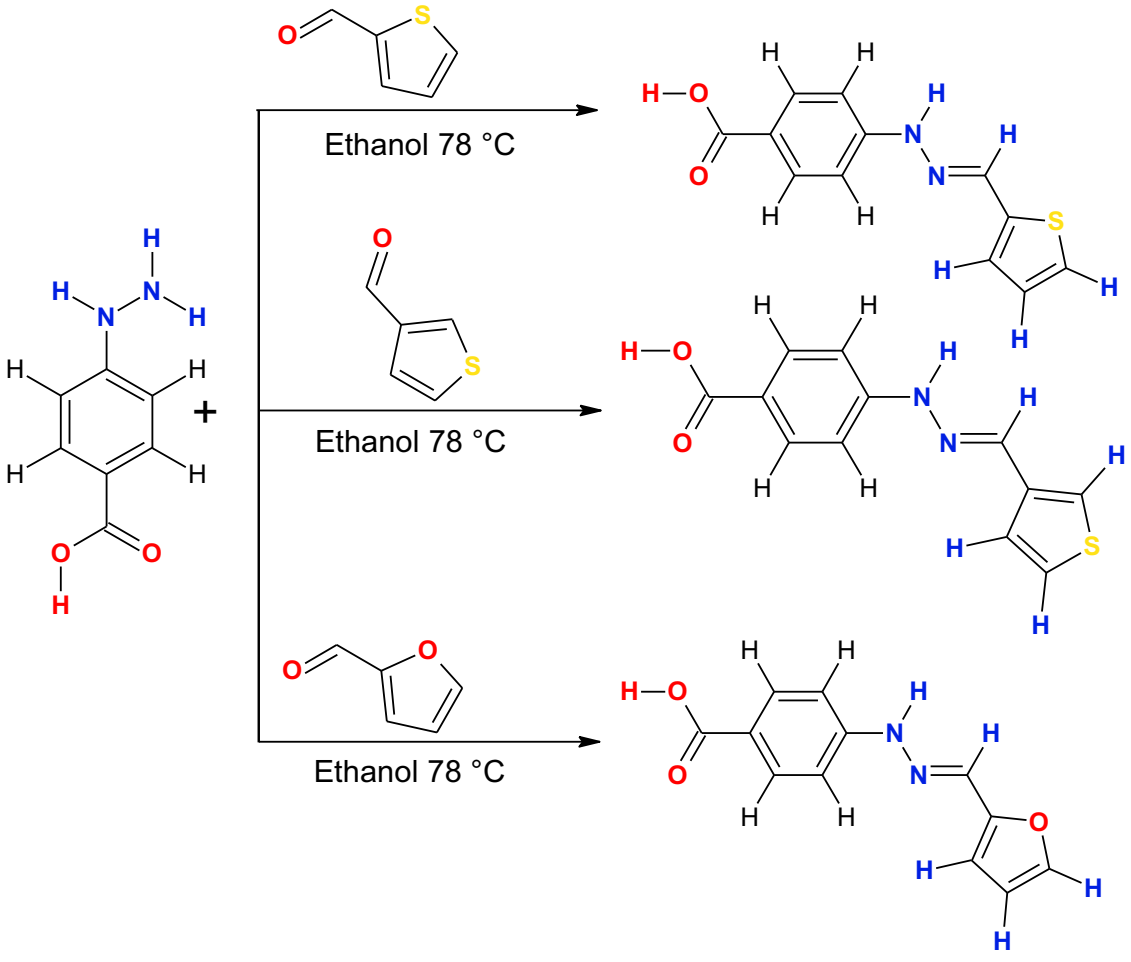


**Fig. 1.** Synthetic rout of the studied hydrazone derivatives.

carbaldehyde 98% in ethanol. The mixture was refluxed for 12 h at a temperature of 78 °C (Fig. 1). The obtained crude solution was cooled at room temperature and it remained clear until the formation of a solid precipitate. The resulting solid is purified by crystallization using ethanol. The yellow solid hydrazone is produced in yield 77%. MF: $C_{12}H_{10}N_2O_2S$, M.p. 252.1 °C, UV–Vis (Methanol), $\lambda_{max}$ (nm): 346. IR (ATR, $\nu(cm^{-1})$): 3524 (O–H), 3313 (N–H), 3282 (C–$H_{Ar}$), 2954 (C–$H_{Alph}$), 1654 (C = O), 1593 (N = C), 1541 (C–H), 1268 (C–N), 1150 (N–N), 1091 (C–O), 852 (C-S), 627 (N–H). **$^1$H NMR** (400 MHz, DMSO, $\delta$(ppm)): 7.09 (s, 1H, -C **H**$_{Ar15}$), 7.53 (s, 1H, -C **H**$_{Ar11}$-S), 7.58 (d, 2H, C **H**$_{Ar2-}$C **H**$_{Ar3}$), 7.73 (s, 1H, C **H**$_{Ar4}$-S), 7.82 (d, 2H, C **H**$_{Ar4-}$C **H**$_{Ar5}$), 8.01 (s, 1H, C **H**=NH), 10.64 (s, 1H, -N **H** –N), 11.91 (s, 1H, O**H**) ; **$^{13}$C NMR**: (75 MHz, DMSO, $\delta$(ppm)): 111.54 (d, 2C, **C**$H_{Ar2-}$ **C**$H_{Ar3}$), 120.55 (s, 1C, **C**$_{Ar6}$), 125.12 (s, 1C, **C** $H_{Ar11}$-S), 125.16 (s, 1C, **C**$H_{Ar13}$), 127.61 (s, 1C, **C**$H_{Ar14}$-S), 131.64 (d, 2C, **C**$_{Ar4-}$ **C**$_{Ar5}$), 135.63 (s, 1C, **C**$H_{Ar15}$), 138.82 (s, 1C, **C**$_{16}$=*N*-), 149.38 (s, 1C, **C**$_{Ar1-}$NH), 167.77 (s, 1C, **C**OOH) ; **$^{15}$N NMR**, DMSO, $\delta$(ppm) : 147.15 (s, 2 N, - **N**H– **N**=C).

### 2.2.3. 4-{(2E)–2-[(furan-2-yl)methylidene]hydrazinyl}benzoic acid (HYDZ-3)

The synthesis was performed according to the same procedure as before, in which we dissolved 1.0 mmol 4-hydrazinybenzoic acid 97% and 1.0 mmol 2-furaldehyde 99% in ethanol. The mixture was refluxed at a temperature of 78 °C for 4 h. The resulting crude precipitate was purified by crystallization in methanol. The obtained yellow solid hydrazone is produced in yield 77%. MF: $C_{12}H_{10}N_2O_3$, M.p. 187.9 °C; UV–Vis (Methanol), $\lambda_{max}$ (nm): 354. IR (ATR, $\nu(cm^{-1})$) : 3564 (O–H), 3312 (N–H), 3277 (C–$H_{Ar}$), 2975 (C–$H_{Alph}$), 1650 (C = O), 1590 (N=$C_{Ar}$), 1527 (C–H), 1272 (C–N), 1162 (N–N), 1095 (C–O), 674 (N–H). **$^1$H NMR** (400 MHz, DMSO, $\delta$(ppm)): 6.58 (s, 1H, -C **H**$_{Ar13}$), 6.74 (s, 1H, C **H**$_{Ar11}$), 7.06 (d, 2H, C **H**$_{Ar2-}$C **H**$_{Ar3}$), 7.75 (s, 1H, C**H**$_{Ar12-}$O), 7.83 (d, 2H, C **H**$_{Ar4-}$C **H**$_{Ar5}$), 7.85 (s, 1H, CH=N-), 10.75 (s, 1H, -N **H** –N), 12.23 (s, 1H, O **H**) ; **$^{13}$C NMR**: (75 MHz, DMSO, $\delta$(ppm)): 110.77 (s, 1C, **C**$H_{Ar11}$), 111.60 (d, 2C, **C**$H_{Ar2-}$ **C**$H_{Ar3}$), 112.42 (s, 1C, **C**$H_{Ar13}$), 120.87 (s, 1C, **C**$_{Ar6}$), 129.98 (s, 1C, **C**$H_{Ar12-}$O), 131.66 (d, 2C, **C**$_{Ar4-}$ **C**$_{Ar5}$), 144.22 (s, 1C, **C**$_{Ar14}$=*N*-), 149.07 (s, 1C, **C**$_{Ar9-}$O), 150.76 (s, 1C, **C**$_{Ar1-}$NH), 167.73 (s, 1C, **C**OOH) ; **$^{15}$N NMR**, DMSO, $\delta$(ppm) : 148.63 (s, 2 N, - **N**H– **N**=C).

### 2.3. Characterization

The synthesized molecules have been characterized by spectroscopic and physicochemical methods such as UV–Vis, IR, $^1$H NMR, $^{13}$C NMR, $^{15}$N NMR and melting point. The open capillary technique in BÜCHI melting point B-540 was used to determine the melting point of the synthesized compounds. The UV–Vis spectra were evaluated in methanol solution using a Jasco V-650 spectrometer in range of 190–900 nm. Also, IR spectra of the synthesized molecules were realized in solid state at room temperature using the JASCO 4000 FTIR spectrometer in the region of 600–4000 $cm^{-1}$. The NMR spectra were realized on a Bruker AVANCE III HD with sande BBO liquid at 400 MHz for $^1$H NMR, $^{13}$C NMR and $^{15}$N NMR in DMSO–$d_6$ as a dissolvable.

### 2.4. DFT calculations

Recently, DFT calculations are considered the most generally utilized computational techniques because of their precision and less time utilization. In this context, the Gaussian 09 W program was utilized to perform all quantum chemical computations. Also, the DFT method at the B3LYP/6–311++*G*(d,p) level has been utilized to calculate the optimized molecular structures of **HYDZ-1, HYDZ-2** and **HYDZ-3** (Fig. 6) [42]. In addition, the calculated vibrational frequencies have been obtained at the optimized structures of the investigated hydrazones. On the other hand, the Time-dependent DFT (TD-DFT) with the B3LYP/6–311++*G*(d,p) method has been used to predict the electronic spectra of the studied hydrazones derivatives in methanol as solvent. The energy gap ($\Delta E_{GAP}$), electrophilicity index ($\omega$), dipole momentum ($\mu$), global softness ($\sigma$), global hardness ($\eta$) and absolute electronegativity ($\chi$) are calculated using the obtained values of energies of HOMO and LUMO orbitals. All these parameters are calculated using the following equations [43–45]:

$$\Delta E_{GAP} = E_{LUMO} - E_{HOMO} \quad (1)$$

$$\eta = \frac{E_{LUMO} - E_{HOMO}}{2} \quad (2)$$

$$\sigma = \frac{1}{\eta} \quad (3)$$

$$\chi = \frac{-(E_{LUMO} + E_{HOMO})}{2} \quad (4)$$

$$\omega = \frac{\chi 2}{2\eta} \quad (5)$$

### 2.5. In vitro biological evaluation

The antioxidant activity of the synthesized hydrazones was evaluated *in vitro* using DPPH [46], ABTS [47], CUPRAC [48], FRAP [49] and phenantroline [50] assays. In these procedures, the methanol was used as a negative control, while BHA (butylated hydroxyanisole), BHT (butylated hydroxytoluene) and ascorbic acid were used as standards. All assays were performed in 96-well microplates using Perkin Elmer, Enspire microplate reader, in triplicate.

The *in vitro* antibacterial activity of these molecules was tested against four ATTC bacterial gram positive and Gram negative strains: *Bacillus subtilis* (ATCC-6633), *Staphylococcus aureus* (ATCC-6538P), *Escherichia coli* (ATCC-8739) and *Pseudomonas aeruginosa* (ATCC-9027). It was determined by the agar disk diffusion method [51,52]. First, the stock solution of the molecules tested was prepared by dissolving 1 mg of the product in 1 ml of DMSO, and then dilutions of 1, 2, 3 and 4 mg/ml were made. Filter paper discs of 5 mm of diameter were impregnated with the corresponding dilutions then are placed on the inoculated MH agar seeded previously by swabbing by an inoculum of $\approx 10^8$ cells/ml of a young culture (18–24 h) of the strain tested. Petri dishes are then pre-incubated for 1/2 h at room temperature, allowing the complete diffusion of the product and then incubated at 37 °C for 24 h. The antibacterial activity was determined by measuring of inhibition zone diameters (mm); a seeding from the zone of inhibition is used to determine whether the activity is bacteriostatic or bactericidal. Gentamicin (10 µg) was used as a positive control and DMSO as a negative one.

Furthermore, it is well known in drug development that the absorption, distribution, metabolism, excretion and toxicity (ADME-T) properties of molecules are one of the main reasons for their failure in clinical trials. The ADME-T properties of the synthesized hydrazones and their pharmacokinetic parameters were evaluated and calculated using OSIRIS and Mol inspiration online property calculation toolkit (available at: http://www.molinspiration.com) [53].

### 2.6. Molecular docking

One of the best ways to understand the binding interaction of ligands and proteins in drug design industry is molecular docking research. Also, molecular docking is one of the best simulation methods for estimating complex of drug-target interactions by

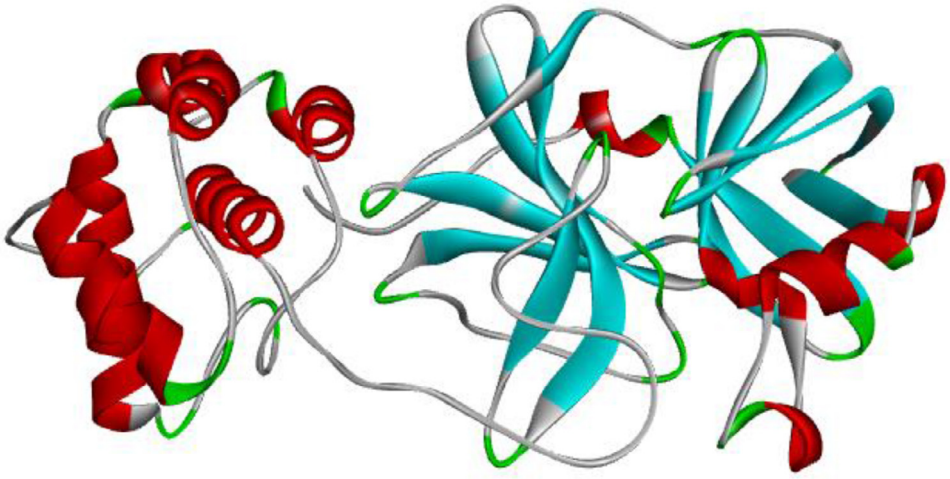

**Fig. 2.** Crystal structure of SARS-CoV-2 main protease.

calculating energy minimization and binding energy [54,55]. The completion of the molecular docking check is to evaluate the binding affinity of the synthetic ligands to the SARS-CoV-2 main protease. The crystal structure of Mpro was provided from the PDB protein data base through code of 6LU7 (Fig. 2). Also, the optimized geometries of **HYDZ-1, HYDZ-2** and **HYDZ-3** obtained by DFT method at the B3LYP/6–311++*G*(d,p) level have been used in molecular docking calculations. Therefore, the molecular docking process has been executed by means of the iGEMDOCK program version 2.1. On the other hand, the obtained HYDZ-1/Mpro, HYDZ-2/Mpro and HYDZ-3/Mpro complexes were visualized with Accelry's Discovery Studio Visualizer version 16.1.0 [38].

## 3. Results and discussion

### 3.1. Spectral analysis

#### 3.1.1. Analysis of the UV–Vis spectra

Generally, the examination of the resulting experimental and calculated UV–Vis spectra (Fig. 3) of **HYDZ-1, HYDZ-2** and **HYDZ-3** recorded in methanol at room temperature indicate the presence of absorption bands in the ultraviolet region.

The experimental spectra of **HYDZ-1, HYDZ-2** and **HYDZ-3** illustrate bands at 202 nm, 204 nm and 204 nm, respectively, corresponded to the $n\rightarrow\pi^*$ transitions produced by the carboxylic acid group (-COOH), where electrons are jump from *n* no bonding orbitals to $\pi$ anti-bonding orbitals. Also, the observed shoulders at 225 nm, 228 nm and 237 nm, respectively, are corresponded to the $n\rightarrow\sigma^*$ transitions created by oxole and thiole groups [56]. On the other hand, the appeared bands at 269 nm, 276 nm and 269 nm, respectively, are related to the $\pi\rightarrow\pi^*$ transitions of the C=C group of the aromatic ring. The obtained shoulders at 300 nm, 302 nm and 303 nm, respectively, represent the $n\rightarrow\pi^*$ transitions associated to the (N–NH) group [25]. Finally, the UV–Vis spectra of the three hydrazones reveal a broad band at 363 nm, 346 nm and 354 nm, respectively, which are related to the $n\rightarrow\pi^*$ transitions produced by the imine group (C=N) [38].

#### 3.1.2. Vibrational analysis

The experimental and calculated IR spectra of **HYDZ-1, HYDZ-2** and **HYDZ-3** are presented in Fig. 4. Also, the obtained vibrational frequencies and their vibrational mode assignments groups are presented in Table 1. On the other hand, a scaling factor of 0.9614 has been used to scale the calculated frequencies [57]. The examination of the results of Table 1 shows that the scaled theoretical frequencies are in good harmony with the experimental frequencies. The investigation of the experimental spectra of the synthesized hydrazones shows the existence of the following vibrational modes:

*3.1.2.1. 4-{(2E)–2-[(*thiophen-2-yl)methylidene*]hydrazinyl}benzoic acid.* According to Fig. 4, the small peaks at 3502 and 3311cm$^{-1}$ are attributed to the O–H and N–H stretching vibrations, respectively. A weak peak appeared at 3276 cm$^{-1}$ can be referred to the

**Table 1**
Experimental and theoretical frequencies of selected vibrations of **HYDZ-1, HYDZ-2** and **HYDZ-3**.

| Compounds | HYDZ-1 | | | HYDZ-2 | | | HYDZ-3 | | |
|---|---|---|---|---|---|---|---|---|---|
| Assignement | Experimental frequencies (cm$^{-1}$) | Calculated frequencies (cm$^{-1}$) | | Experimental frequencies (cm$^{-1}$) | Calculated frequencies (cm$^{-1}$) | | Experimental frequencies (cm$^{-1}$) | Calculated frequencies (cm$^{-1}$) | |
| | | Unscaled | Scaled | | Unscaled | Scaled | | Unscaled | Scaled |
| $_{(N-H)}$ | 3311 | 3497 | 3362 | 3313 | 3516 | 3380 | 3312 | 3498 | 3362 |
| $\nu_{(C-H)Ar}$ | 3276 | 3248 | 3314 | 3282 | 3238 | 3113 | 3277 | 3244 | 3118 |
| $\nu_{(C-H)Alph}$ | 2930 | 3029 | 2912 | 2954 | 3153 | 3031 | 2975 | 3049 | 2931 |
| $\nu_{(C=O)}$ | 1661 | 1773 | 1704 | 1654 | 1774 | 1705 | 1650 | 1773 | 1704 |
| $\nu_{(C=N)}$ | 1593 | 1646 | 1582 | 1593 | 1651 | 1587 | 1590 | 1643 | 1579 |
| $\nu_{(C-N)}$ | 1273 | 1295 | 1245 | 1268 | 1291 | 1241 | 1272 | 1296 | 1245 |
| $_{(N-N)}$ | 1138 | 1193 | 1146 | 1150 | 1097 | 1054 | 1162 | 1218 | 1170 |
| $\nu_{(C-O)}$ | 1090 | 1091 | 1048 | 1091 | 1090 | 1047 | 1095 | 1102 | 1059 |
| $\nu_{(C-S)}$ | 852 | 858 | 824 | 852 | 823 | 791 | – | – | – |
| $\rho_{out(C-H)}$ | 762 | 701 | 673 | 771 | 652 | 626 | 734 | 743 | 714 |
| $\rho_{out(N-H)}$ | 685 | 642 | 617 | 627 | 442 | 424 | 674 | 500 | 480 |

$\nu$: stretching, $\rho_{out}$: out of plane bending.

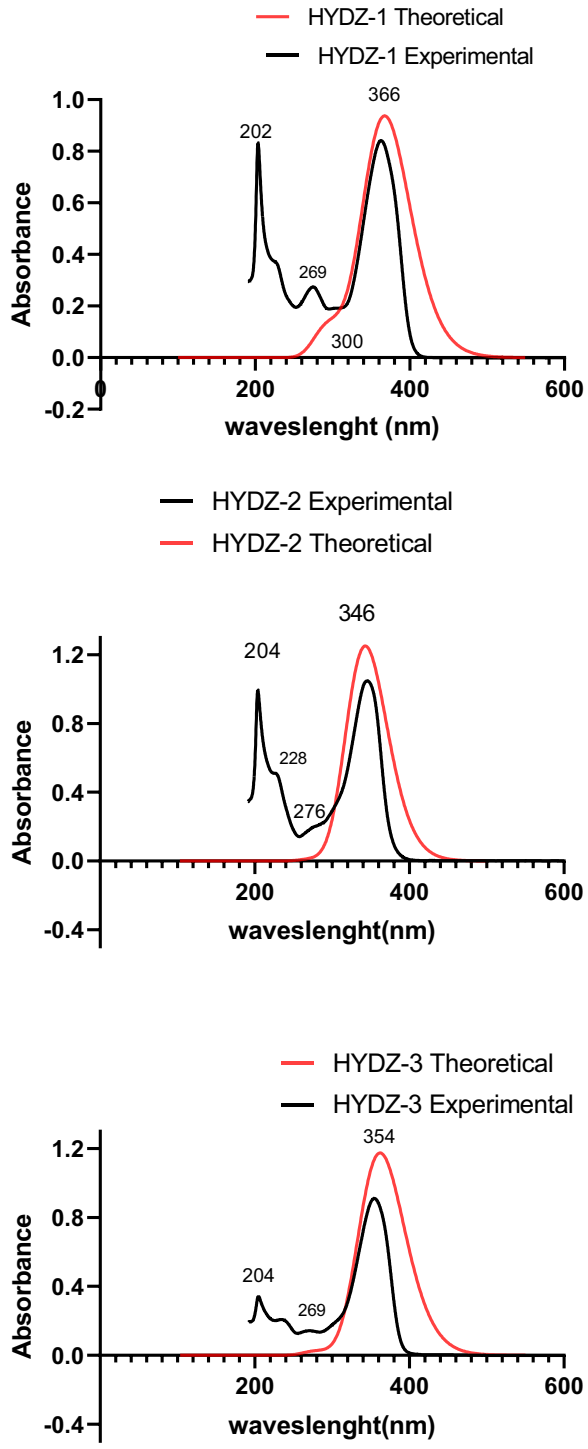


**Fig. 3.** Theoretical and experimental UV–Vis spectra of HYDZ-1, HYDZ-2 and HYDZ-3.

stretching vibration of aromatic C–H groups. The stretching vibrations of aliphatic C–H groups are corresponded to the less intense peak appeared at 2930 $cm^{-1}$. The presence of peaks within the range of 1600–2000 $cm^{-1}$ is mostly due to the bending vibration of the C=N or aromatic C=C groups. The characteristic peak of **HYDZ-1** is observed as a very intense peak at 1593 $cm^{-1}$ which is assigned to the stretching vibration of the imine group (C=N). In addition, peaks with medium intensities obtained within the region 1200–1273 $cm^{-1}$ can be explaining the vibration of C–N groups. The detected peaks in the region 1100–1138 $cm^{-1}$ could be assigned to the presence of the N–N functional group. The intense thin peak located at 685 $cm^{-1}$ may be due to N–H bending vibration [25,58].

*3.1.2.2. 4-{(2E)–2-[(*thiophen-3yl*)*methylidene*]hydrazinyl}benzoic acid.* The week peaks located at 3524 and 3313 $cm^{-1}$ could be attributed to the O–H and N–H stretching vibrations, respectively. A small peak appeared at 3282 $cm^{-1}$ can be presents the vibration of aromatic C–H groups. The stretching vibrations of the aliphatic C–H groups are corresponded to the less intense peak appeared at 2954 $cm^{-1}$. The presence of peaks within the range of 1600–2000 $cm^{-1}$ is mostly due to the bending vibration of the C=N or aromatic C=C functional groups. The characteristic peak of **HYDZ-2** is observed as a very intense peak at 1593 $cm^{-1}$ which is assigned to the stretching vibration of the hydrazone group (C=N–N). In addition, peaks with medium intensities obtained within the region 1200–1268 $cm^{-1}$ can be explaining the vibration of C–N group. The observed peaks in the region 1100–1150 $cm^{-1}$ present the vibration of the N–N functional group. The N–H bending vibration is observed as an intense thin peak at 627 $cm^{-1}$.

*3.1.2.3. 4-{(2E)–2-[(*furan-2-yl*)*methylidene*]hydrazinyl}benzoic acid.* The small peaks situated at 3564 and 3312 $cm^{-1}$ are attributed to the stretching vibrations of O–H and N–H groups, respectively. Also, the stretching vibrations of aromatic C–H groups are appeared as a weak peak at 3277 $cm^{-1}$. On the other hand, the stretching vibrations of aliphatic C–H groups are observed as a less intense peak at 2975 $cm^{-1}$. Generally, the bending vibrations of the C=N and aromatic C=C groups are obtained within the range of 1600–2000 $cm^{-1}$. The very intense peak located at 1590 $cm^{-1}$ represents the characteristic peak of **HYDZ-3**, which is referred to the stretching vibration of the imine group (C=N). Moreover, the stretching vibrations of the C–N group are appeared as medium peaks within the region of 1200–1272 $cm^{-1}$. Generally, the characteristic peaks of the N–N group vibrations are situated between 1100 and 1162 $cm^{-1}$. Finally, the intense thin peak sited at 674 $cm^{-1}$ may be associated to the N–H bending vibration.

Fig. 5 shows the linear fit of the variation of scaling theoretical frequencies *versus* experimental results. Generally, straight lines have been obtained between theoretical and experimental frequencies with correlation coefficients of correlation coefficients of $R^2$ = 0.9957, $R^2$ = 0.9926 and $R^2$ = 0.9932, respectively, of **HYDZ-1, HYDZ-2** and **HYDZ-3**. We observe that the obtained values of $R^2$ are approximately equal to 1, indicating that the scaling theoretical frequencies are in good agreement with the experimental frequencies.

*3.1.3. NMR analysis*

The examination of the NMR results of **HYDZ-1, HYDZ-2** and **HYDZ-3** (Table 2 and Fig. S3) recorded in DMSO–$d_6$ at room temperature permits to determine the following characteristic signals:

From $^1$H NMR results of **HYDZ-1, HYDZ-2** and **HYDZ-3**, the observed signals between 6.58 and 7.83 ppm are attributed to the

**Table 2**
Experimental $^1$H NMR and $^{13}$C NMR chemical shifts ($\delta$ in ppm) of **HYDZ-1, HYDZ-2** and **HYDZ-3**.

| HYDZ-1 | | HYDZ-2 | | HYDZ-3 | |
|---|---|---|---|---|---|
| $^1$H NMR | $^{13}$C NMR | $^1$H NMR | $^{13}$C NMR | $^1$H NMR | $^{13}$C NMR |
| 7.01 | 111.54 | 7.09 | 111.54 | 6.85 | 110.73 |
| 7.10 | 120.84 | 7.53 | 120.55 | 6.74 | 111.60 |
| 7.30 | 127.13 | 7.58 | 125.12 | 7.06 | 112.42 |
| 7.55 | 128.17 | 7.73 | 125.16 | 7.75 | 120.87 |
| 7.83 | 128.30 | 7.82 | 127.61 | 7.83 | 129.98 |
| 8.15 | 131.69 | 8.01 | 131.64 | 7.85 | 131.66 |
| 10.75 | 134.93 | 10.64 | 135.63 | 10.75 | 144.22 |
| 12.73 | 140.71 | 11.91 | 138.82 | 12.29 | 149.07 |

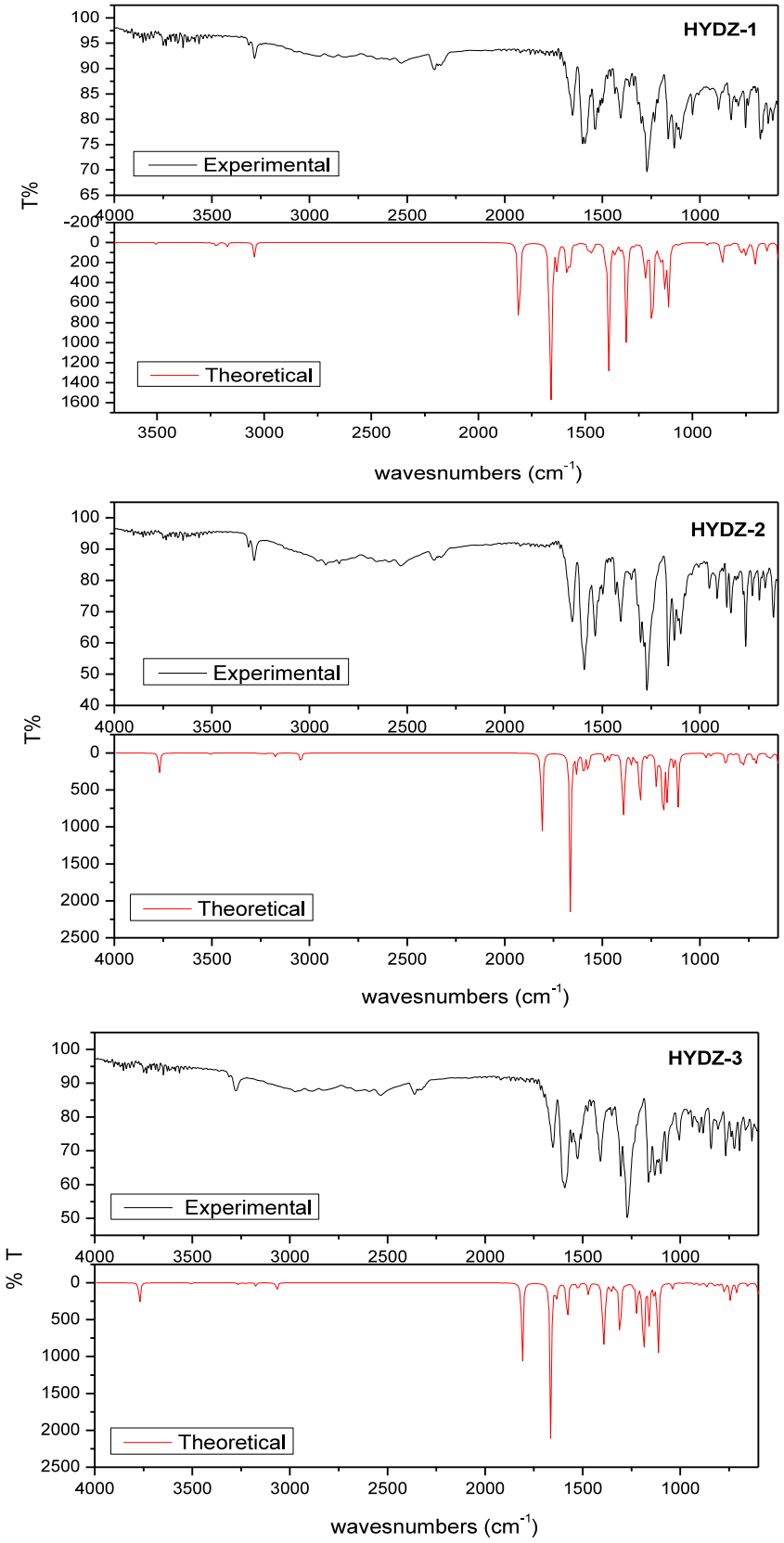


**Fig. 4.** Experimental and calculated IR spectra of HYDZ-1, HYDZ-2 and HYDZ-3.

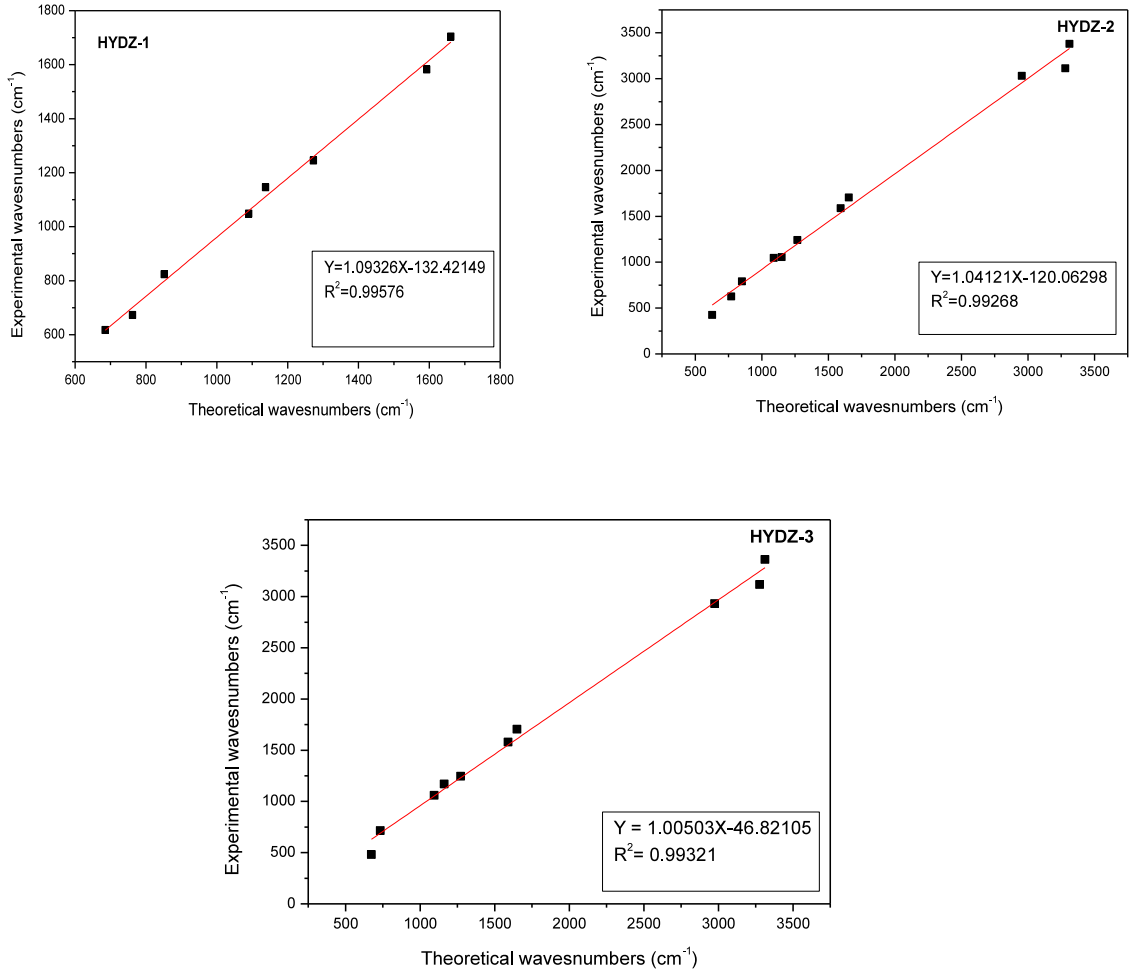


**Fig. 5.** Correlation diagrams between the theoretical and experimental wavenumbers of HYDZ-1, HYDZ-2 and HYDZ-3.

aromatic protons (C **H**$_{Ar\text{-benzene}}$ and C **H**$_{Ar\text{-heterocyclic}}$). The proton of the hydrazone group (C **H**=N–N) appears as a single signal at 8.15, 8.01 and 7.85 ppm, respectively. In addition, single signals observed at 10.75, 10.64 and 10.75 ppm, respectively, are related to the proton of the N **H** –N- group. Also, the clarification of the obtained H of the carboxylic acid group (O **H**) was observed as a single signal at 12.23, 11.91 and 12.29 ppm, respectively, for these three molecules [38].

$^{13}$C NMR spectra of the three hydrazones derivatives show that the following characteristic signals are present: the carbon of the ( **C**$_{Ar}$-NH-) group is observed as a single signal at 148.99, 149.38 and 150.76 ppm, respectively. The signal at 128.17, 138.82 and 144.22 ppm can be related to the carbon of the imine group (-N= **C**H-). Also, single signals observed at 167.74, 167.77 and 167.73 ppm, respectively, are related to the carbon atom of the carboxylic acid group ( **C**OOH). On the other hand, the aromatic ring carbon atoms are observed between 110.77 ppm and 140.71 ppm [25].

For the $^{15}$N NMR results, the obtained spectra of **HYDZ-1, HYDZ-2** and **HYDZ-3** (Fig. S3) show the presence of the following characteristic signals: single intense signals appeared at 147.71, 147.15 and 148.63, respectively, are attributed to the two nitrogen atoms of the hydrazone group (- **N**H– **N**=C).

### 3.2. DFT study

Table 3 combines the obtained values of the chemical reactivity descriptors of the synthesized hydrazones determined by DFT calculations, such as total energy ($E_{Tot}$), energy gap ($\Delta E_{GAP}$), dipole momentum ($\mu$), electrophilicity ($\omega$) and chemical hardness ($\eta$) [59,60].

**Table 3**
Global chemical reactivity descriptors for **HYDZ-1, HYDZ-2** and **HYDZ-3** calculated by DFT method at B3LYP/6–311++*G*(d,p).

| Quantum chemical descriptors | HYDZ-1 | HYDZ-2 | HYDZ-3 |
|---|---|---|---|
| $E_{Tot}$ (eV) | −30,521.49432 | −30,521.364 | −21,732.7029 |
| $E_{HOMO}$ (eV) | −5.70487 | −5.9002 | −5.6689 |
| $E_{LUMO}$ (eV) | −2.061263 | −1.8198 | −1.9548 |
| $\Delta E_{GAP}$ (eV) | 3.6436 | 4.0804 | 3.7141 |
| $\mu$ (Debye) | 4.4728 | 5.5653 | 4.4565 |
| $\eta$ (eV) | 1.8218 | 2.0402 | 1.8570 |
| $\sigma$ | 0.5489 | 0.4901 | 0.5385 |
| $\chi$ (eV) | 3.8830 | 3.860 | 3.8118 |
| $\omega$ | 4.1382 | 3.6515 | 3.9122 |

#### 3.2.1. Optimized molecular structures

According to the values of the total energy calculated at the optimal geometries of the studied compounds (Table 4), we observe that **HYDZ-2** presents the minimum value of $E_{Tot}$, which indicates that the conformation of **HYDZ-2** presented in Fig. 6 is more stable than these of **HYDZ-3** and **HYDZ-1**. Also, we can be seen from Table 3 that the value of the $\Delta E_{GAP}$ of **HYDZ-1** is low than these of **HYDZ-2** and **HYDZ-3**, indicating that the **HYDZ-1** has the good chemical reactivity and the lowest stability which indicate that the

**Table 4**
Atomic NBO charges of **HYDZ-1, HYDZ-2** and **HYDZ-3** calculated by DFT method at B3LYP/6–311++*G*(d,p).

| HYDZ-1 | | HYDZ-2 | | HYDZ-3 | |
|---|---|---|---|---|---|
| Symbol | NBO Charge | Symbol | NBO Charge | Symbol | NBO Charge |
| C1 | −0.2196900 | **C1** | −0.3600700 | **C1** | 0.2420600 |
| C2 | −0.2457100 | **S2** | 0.4482700 | **O2** | −0.4609100 |
| C3 | −0.2439300 | **C3** | −0.1716300 | **C3** | −0.2562800 |
| S4 | 0.4259500 | **C4** | −0.3762300 | **C4** | 0.1305300 |
| C5 | −0.3827100 | **C5** | −0.2621100 | **C5** | −0.2944000 |
| C6 | 0.0257600 | **C6** | 0.0447000 | **C6** | 0.0077900 |
| H7 | 0.2199800 | **C7** | −0.2430600 | **C7** | −0.2448700 |
| H8 | 0.2267800 | **C8** | −0.1258000 | **C8** | −0.1250500 |
| C9 | −0.2444200 | **C9** | 0.1904000 | **C9** | 0.1872100 |
| C10 | −0.1249300 | **C10** | −0.2055000 | **C10** | −0.2061700 |
| C11 | 0.1877300 | **C11** | −0.2491000 | **C11** | −0.2489400 |
| C12 | −0.2062300 | **C12** | −0.1409600 | **C12** | −0.1402900 |
| C13 | −0.2489400 | **C13** | 0.7855200 | **C13** | 0.7850000 |
| C14 | −0.1400200 | **O14** | −0.6124800 | **O14** | −0.6127000 |
| C15 | 0.7850000 | **O15** | −0.6979600 | **O15** | −0.6977500 |
| O16 | −0.6126400 | **N16** | −0.4033300 | **N16** | −0.3762900 |
| O17 | −0.6977300 | **N17** | −0.2401700 | **N17** | −0.2366500 |
| N18 | −0.3780000 | **H18** | 0.1945300 | **H18** | 0.2305500 |
| N19 | −0.2395200 | **H19** | 0.2300800 | **H19** | 0.2286600 |
| H20 | 0.2303400 | **H20** | 0.2295300 | **H20** | 0.2028600 |
| H21 | 0.2286700 | **H21** | 0.2257700 | **H21** | 0.2253900 |
| H22 | 0.2028800 | **H22** | 0.2331300 | **H22** | 0.4836000 |
| H23 | 0.2253700 | **H23** | 0.2283000 | **H23** | 0.3559200 |
| H24 | 0.4836100 | **H24** | 0.2029600 | **H24** | 0.2308000 |
| H25 | 0.3553200 | **H25** | 0.2248100 | **H25** | 0.2238900 |
| H26 | 0.2289000 | **H26** | 0.4834000 | **H26** | 0.1978500 |
| H27 | 0.1581900 | **H27** | 0.3670100 | **H27** | 0.1681800 |

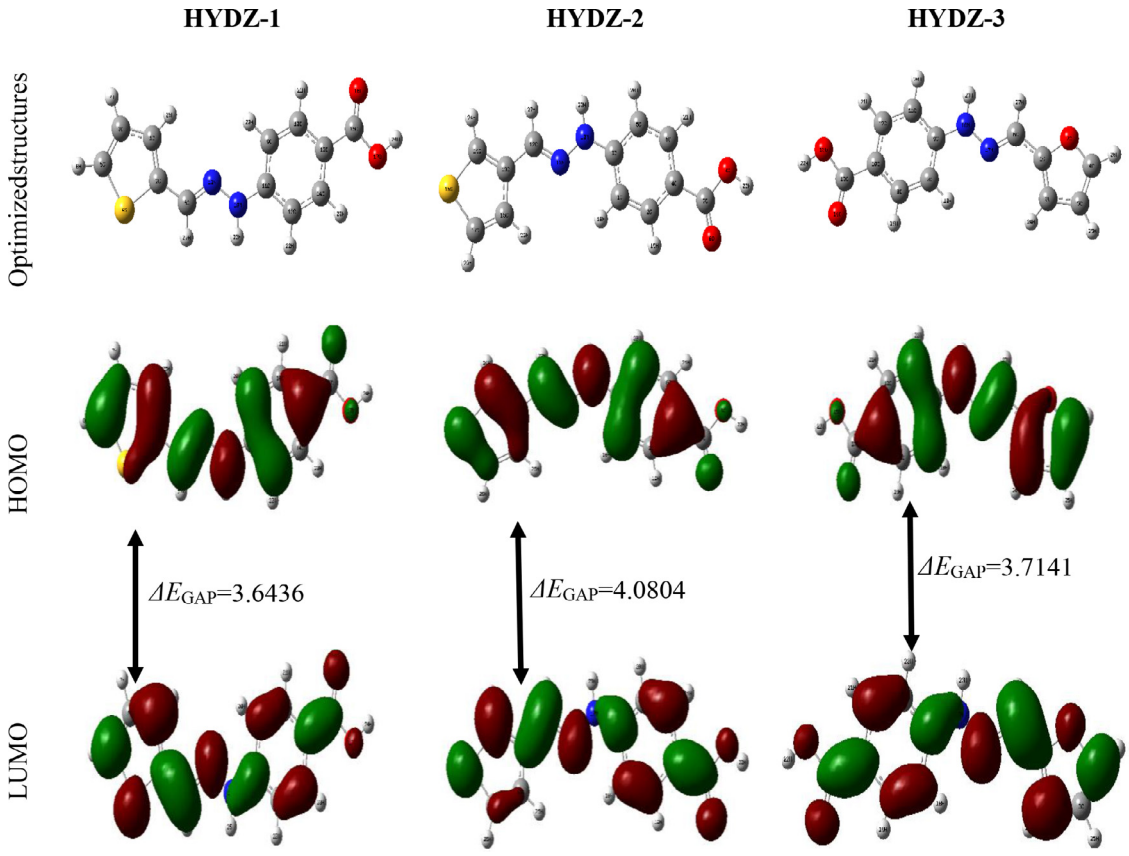


**Fig. 6.** Optimized molecular structures and frontier molecular orbitals density distributions of HYDZ-1, HYDZ-2 and HYDZ-3.

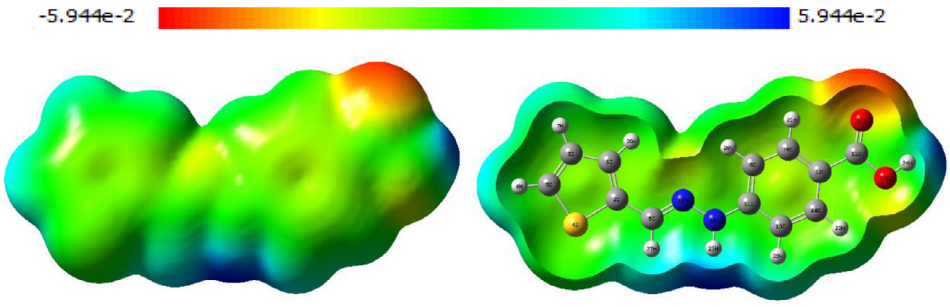


HYDZ-1

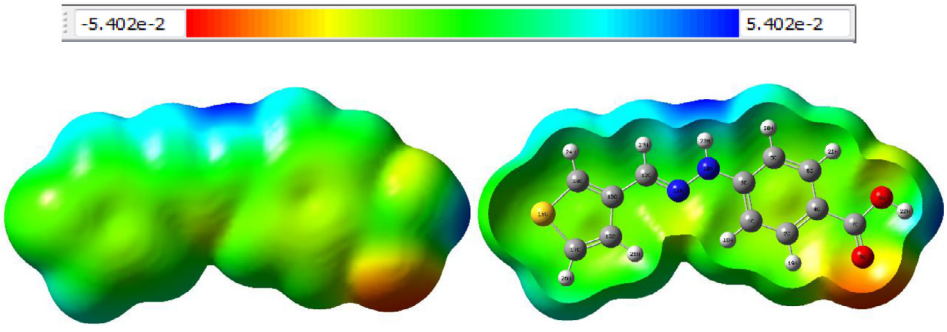


HYDZ-2

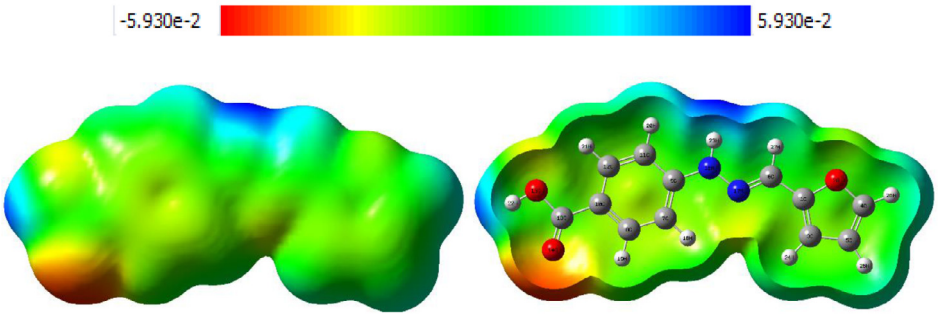


HYDZ-3

**Fig. 7.** Molecular electrostatic potential maps of HYDZ-1, HYDZ-2 and HYDZ-3.

**Table 5**
Determination of the antioxidant activity of the examined hydrazone derivatives by DPPH, ABTS, CUPRAC, FRAP and Phenantroline assays.

| Compounds | $DPPHIC_{50}$ mM[a] | $ABTSIC_{50}$ mM[a] | $CUPRACA_{0.50}$ mM[a] | $FRAPA_{0.50}$ mM[a] | $PhenanthrolineA_{0.50}$ mM[a] |
|---|---|---|---|---|---|
| **HYDZ-1** | 87.91±3.34 | 8.29±0.32 | 49.23±1.2 | 41.12±0.40 | 11.49±1.45 |
| **HYDZ-2** | 143.07±1.30 | 7.46±0.39 | 31.59±0.30 | 77.40±0.30 | 14.06±0.87 |
| **HYDZ-3** | 38.33±0.81 | 1.27±0.10 | 30.95±1.05 | 56.38±0.49 | 15.89±1.12 |
| **BHA**[b] | 24.28±1.28 | 7.67±0.40 | 17.97±0.66 | N.T | 4.31±0.03 |
| **BHT**[b] | 70.9 ± 6.6 | 8.24±0.13 | 16.62±0.79 | N.T | 4.20±0.06 |
| **Ascorbic acid**[b] | N.T | N.T | N.T | 15.39±1.10 | N.T |

[a]Values expressed are means ± S.D. of three parallel measurements. ($p<0.05$). N.T: not tested.
[b]References.

**Table 6**
The antibacterial inhibition diameters in mm.

| Strains | Diameter of the inhibition zones (mm) | | | |
|---|---|---|---|---|
| | HYDZ-1 | HYDZ-2 | HYDZ-3 | GM |
| *P. aeruginosa* | 14±2.08 | 7 ± 0.57 | <5 | 20 |
| *B. subtilis* | <5 | <5 | <5 | 30 |
| *S. aureus* | <5 | <5 | <5 | 25 |
| *E. coli* | <5 | <5 | <5 | 22 |

*GM : gentamicine.

transfer of electrons between HUMO and LOMO is easiest for it and therefore it acts as a better bioactive molecule [61,62].

### 3.2.2. Frontier molecular orbitals analysis

The stability and the chemical reactivity of bioactive compounds can be explained extensively via HOMO and LUMO orbitals and their energies [38]. Generally, a high value of $E_{HOMO}$ is related to the electron donor ability of the molecule [63], while a higher value of the $E_{LUMO}$ is related to the molecule ability to accept electrons [64]. Fig. 6 shows that the electron densities of the HOMO and LUMO orbitals are almost dispersed on the entire molecular structures of **HYDZ-1, HYDZ-2** and **HYDZ-3**. On the other hand, the positive phases of each molecule are colored in red solid surfaces, while the negative phases are colored in green [33]. The HOMO densities are related to the strong electronegativity of oxygen and sulfur atoms. It was disturbed on the thiophene, furan ring and C=N function which have larger affinity to conserve their electronic pairs [25]. The high HOMO energy corresponds to a high capacity to lose an electron, whereas the smaller LUMO energy indicates the greatest affinity for electrons. We observe from Table 3, the order of $E_{HOMO}$ is **HYDZ-3** (−5.6689) > **HYDZ-1** (−5.70487) > **HYDZ-2** (−5.9002), hence **HYDZ-3** has better electron donating ability and liberates electrons more than **HYDZ-1** and **HYDZ-2** which expresses their capacity in antioxidant activity. Also, the lowest value of $E_{LUMO}$ is referred to the **HYDZ-2** (−1.8198) which shows its elevated potential to receive electrons.

Although dipole moment importance as an indicator of the electronic distribution within a molecule is certain, studies have reported inconsistent findings on the association between dipole moment values and the inhibition efficiency of bioactive molecules [65]. In the current study, as expected, we did find this significant association between the dipole moment values and the order of the bioactivity: **HYDZ-2** > **HYDZ-1**> **HYDZ-3**.

The chemical hardness indicates the resistance to deformation or polarization of the electron cloud of atoms, ions or molecules under a small disturbance of the chemical reaction. Also, hard molecules have a high energy gap and soft molecules have a small energy gap [66]. Generally, the low value of the hardness and the high value of the softness of a molecule can produce a high inhibitory efficiency [67]. The hardness and softness of our molecules follow the following order: **HYDZ-1** < **HYDZ-3** < **HYDZ-2** and **HYDZ-1** > **HYDZ-3** > **HYDZ-2**, respectively. These results indicate that the **HYDZ-1** with a lowest hardness and highest softness is the less stable and the most reactive species.

The values of electrophilicity index ($\boldsymbol{\omega}$) of these compounds are between 3.6515 and 4.1382. Generally, the high value of $\boldsymbol{\omega}$ proves better electrical properties, while a low value of $\boldsymbol{\omega}$ indicates poor electrophiles. According to the Table 3, we find that our molecules have better electrophilicity which measures the energy lowering due to the electron flow between the donor and acceptor. Finally, we conclude that **HYDZ-1** has a good inhibiting activity (antibacterial and inhibition of SARS-CoV-2 main protease) and **HYDZ-3** have a good antioxydante activity, while **HYDZ-2** shows a more stable conformer among these compounds.

### 3.2.3. Molecular electrostatic potential surfaces (MEP)

To determine the active sites that lead to electrophilic and nucleophilic attacks, we decided to use the molecular electrostatic potential surfaces (MEP) as a useful descriptor [58]. MEP describes the charge distribution of molecules in a three-dimensional manner, and correlates the total charge distribution with dipole moment, electronegativity, partial charge, and chemically reactive sites of molecules [67]. The zero potential area is represented by green color, and the evolution of potential follows the order of red < orange < yellow < green < blue [68]. Fig. 7 represents the calculated MEP surfaces of **HYDZ-1, HYDZ-2** and **HYDZ-3** with potential ranges of [−5.944 $10^{-2}$, 5.944 $10^{-2}$], [−5.402 $10^{-2}$, 5.402 $10^{-2}$] and [−5.930 $10^{-2}$, 5.930 $10^{-2}$], respectively. So, surfaces under investigation appear in different colors. Generally, red, orange and yellow zones indicate the negative regions of MEP, corresponding to nucleophilic sites (carboxylic, thiophene, furane and hydrazone functional groups). On the other hand, green and blue zones

**Table 7**
Calculated physicochemical and pharmacokinetic parameters (ADME-T) of the synthesized compounds, which important for a good oral bioavailability.

| Compounds | miLogP<5 | solubility | TPSA (oA) <500 | MW | nON<10 | nOHNH<5 | MV | vio | Toxicity risks | | | |
|---|---|---|---|---|---|---|---|---|---|---|---|---|
| | | | | | | | | | Mut | Tumo | Irr | R,E |
| HYDZ-1 | 4.57 | −3.17 | 61.69 | 246.29 | 4 | 2 | 208.83 | 0 | No | No | No | No |
| HYDZ-2 | 4.26 | −3.06 | 61.69 | 246.29 | 4 | 2 | 208.83 | 0 | No | No | No | No |
| HYDZ-3 | 3.93 | −2.84 | 74.83 | 230.22 | 5 | 2 | 199.68 | 0 | No | No | No | No |
| Chloroquine* | 4.01 | -4.06 | 28.16 | 319.88 | 3 | 1 | 313.12 | 1 | Yes | No | Yes | No |
| Hydroxychl-oroquine* | 3.08 | -3.55 | 48.38 | 335.88 | 4 | 2 | 321.38 | 0 | Yes | No | No | No |

*: Drugs Reference, Topological polar surface area (TPSA); Number of rotatable bonds (n-rotb); Molecular weight (MW); Molecular volume (MV); Logarithm of partition coefficient between n-octanol and water (miLogP); Number of hydrogen bond donors (n-OHNH); Number of hydrogen bond acceptors (n-ON); Lipinski's violation (vio) (Mut) mutagenic (Tumo): tumorigenic (Irr) : irritant (R.E) reproductive effective.

**Table 8**
Energy distribution of the investigated hydrazones between van der Waals forces, hydrogen bonding and electrostatic interactions.

| Compounds | Total energy | vdW | H-Bond | Elec |
|---|---|---|---|---|
| Mpro–HYDZ-1 | −89.90 | −70.17 | −17.17 | −2.56 |
| Mpro-HYDZ-2 | −85.66 | −60.75 | −22.03 | −2.88 |
| Mpro-HYDZ-3 | −84.82 | −71.07 | −13.07 | −0.69 |
| Chloroquine* | -83.91 | −74.41 | −9.5 | 0 |
| Hydroxychloroquine* | -82.27 | −67.02 | −15.25 | 0 |

* Drugs Reference**, H-bonds:** hydrogen bonding, **vdW:** van der Waals forces and **Elec**: electrostatic interactions.

present the positive regions responsible for the electrophilic attacks (hydrogen atoms and benzene ring).

### 3.2.4. Atomic charges of HYDZ-1, HYDZ-2 and HYDZ-3 using NBO analysis

In general, the electron density of molecules can be affected by NBO charges. Also, to check bonds and interaction bonds within and between molecules, NBO analysis can be used to evaluate the delocalization of the electron density between occupied Lewis-type orbitals and empty non-Lewis NBOs, indicating the stability of the donor-acceptor interaction [69]. For the investigated hydrazones, the calculated natural atomic charges of all atoms are offered in Table 4. From the obtained results, it can be seen that oxygen and nitrogen atoms have the most negative charges, which is due to molecular relaxation [38]. In addition, the more positive charges are located on the hydrogen atoms. For the studied molecules, the negative charges are located on O16, O17, N18 and N19 atoms for **HYDZ-1**, O14, O15, N16 and N17 atoms for **HYDZ-2** and O2, O14, O15, N16 and N17 atoms for **HYDZ-3**.

## 3.3. Biological activity

### 3.3.1. Evaluation of the antioxidant activity

The $IC_{50}$ and $A_{0.50}$ values were determined for all the compounds and presented in Table 6. In DPPH assay, all tested compounds showed a good antioxidative activity. Also, **HYDZ-3** showed the lowest $IC_{50}$ value among the synthesized hydrazones (38.33 ± 0.81 mM), and presents an antioxidant activity superior to that of the standard BHT (70.9 ± 6.6 mM), and comparable to that of the standard BHA (24.28 ± 1.28 mM). It is therefore possible to conclude that all the prepared hydrazones exhibit a high antioxidant activity ($IC_{50}$ between 38.33 ± 0.81 and 143.07 ± 1.3 mM) [70].

The results attained from ABTS assay attest that all tested compounds exhibit elevated antioxidant activities. In addition, **HYDZ-3** was found to be the best antioxidant agent ($IC_{50}$ 1.27 ± 0.10 mM)). On the other hand, it can be seen from Table 5 that the investigated hydrazone derivatives have an antioxidant activity higher or comparable to that of the standards BHT and BHA.

According to the CUPRAC assay, we can see that all the prepared hydrazones exhibit a comparable antioxidant activity ($A_{0.50}$ between 31.59 ± 0.30 and 49.23 ± 1.2 mM) with that of the standards BHA and BHT (17.97 ± 0.66 mM and 16.62 ± 0.79 mM, respectively).

As to the results of the FRAP assay, our hydrazones derivatives exhibit also a comparable antioxidant activity ($A_{0.5°}$ between 41.12 ± 0.40 and 77.40 ± 0.30 mM) to that of the standard ascorbic acid (15.39 ± 1.10 mM).

Regarding the phenantroline assay, the high antioxidant activity has been observed for **HYDZ-1** with an $A_{0.50}$ value of 11.49 ± 1.45 mM, which demonstrates that it has a good antioxidant activity comparable to that of standards BHA and BHT (4.31 ± 0.03 and 4.20 ± 0.06 µM, respectively).

In summary, from the results of the antioxidant evaluation by DPPH, ABTS, CUPRAC, FRAP and Phenanthroline assays, the following observations can be derived:

- The studies carried out measuring the antioxidant activity did not correlate with each other. This result can be explained by the different mechanisms of action of the assays.
- The prepared hydrazone derivatives exhibited a high antioxidant activity.
- In DPPH and ABTS assay, compound **HYDZ-3** showed a higher antioxidant activity than that of the standards BHA and BHT, due to presence of furan group within hydrazone compounds that exerted an abundant inhibitory effect against various free radicals.

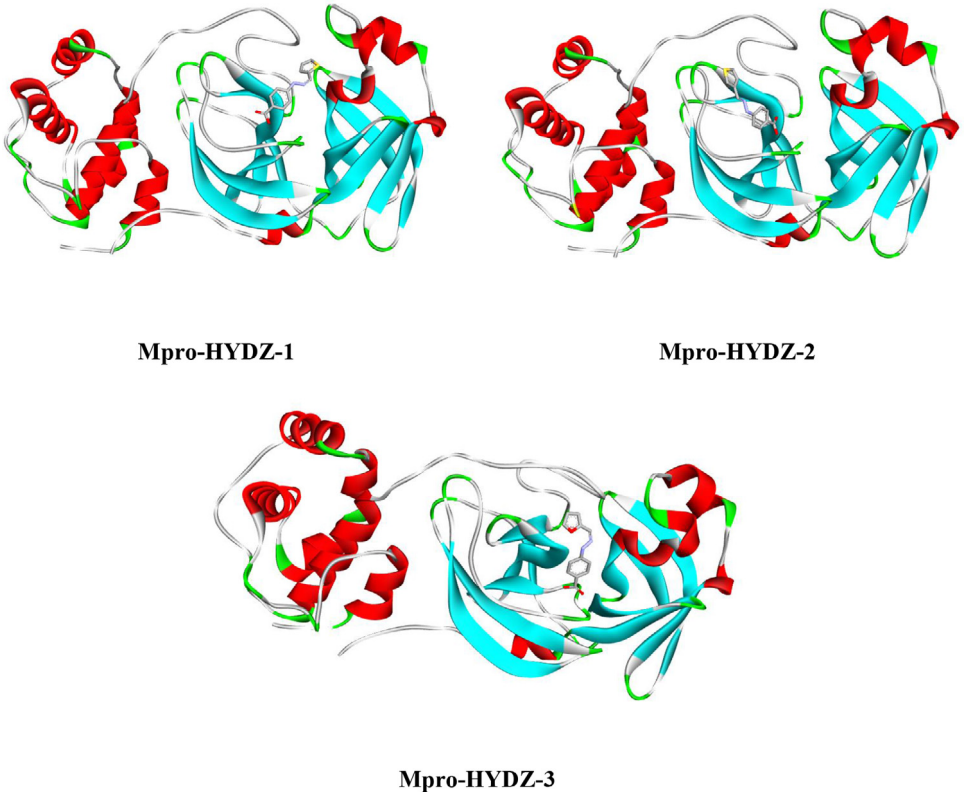


**Fig. 8.** Best docked poses visualization of HYDZ-1, HYDZ-2 and HYDZ-3 with SARS-CoV-2 main protease.

- The thiophene group contributed to the antiradical activity even if it is in position 2 or 3 on the hydrazone moiety (**HYDZ-1** and **HYDZ-2**). It is to be noted that position 2 (**HYDZ-1**) is more reactive than position 3.
- In FRAP and Phenanthroline assays, **HYDZ-1** was regarded as the best antioxidant with comparable value of the standards BHA and BHT because they showed a low value of $E_{Gap}$, which means that it is likely to react more, and the mechanism of this assays is consists in the electron transfer which explains the reactivity of this compound.
- It is well known that the best anti-oxidant activity is observed with **HYDZ-1** and **HYDZ-3** due to the electronic resonance outcome of the hydrazone compounds [71].
- The mechanism of DPPH and ABTS based on the transfer of $H^+$ ($IC_{50}$) and CUPRAC, FRAP phenantroline based on the mechanism of transfer of electrons ($A_{0.5}$) explain the different reactivities of these molecules.
- Finally, except the ABTS assay, the other assays showed a smaller dynamic range in the data. This could also explain the non-correlation of the results.

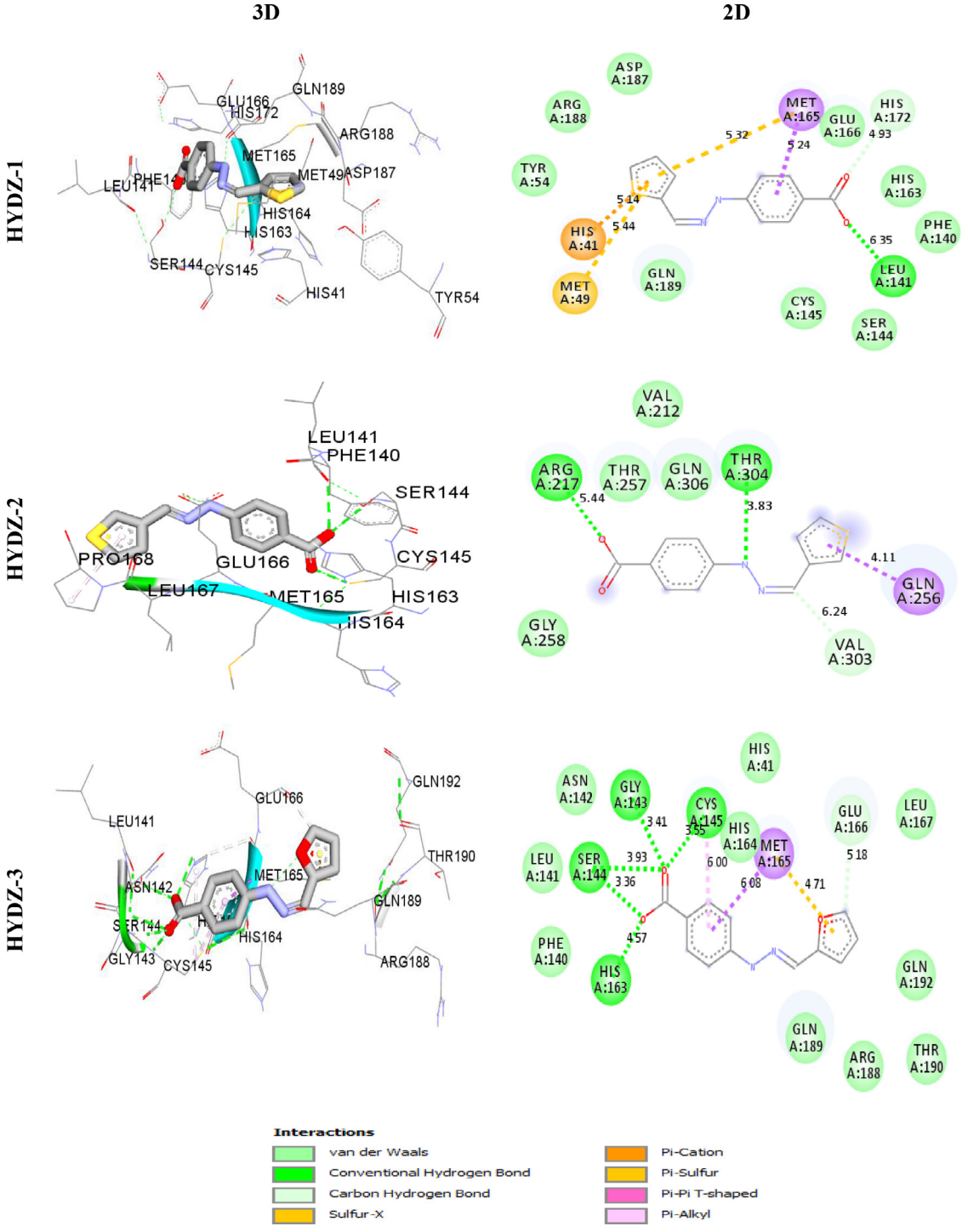


**Fig. 9.** 3D and 2D Binding-interaction diagrams of HYDZ-1, HYDZ-2, HYDZ-3, Chloroquine and Hydroxychloroquine with SARS-CoV-2 main protease.

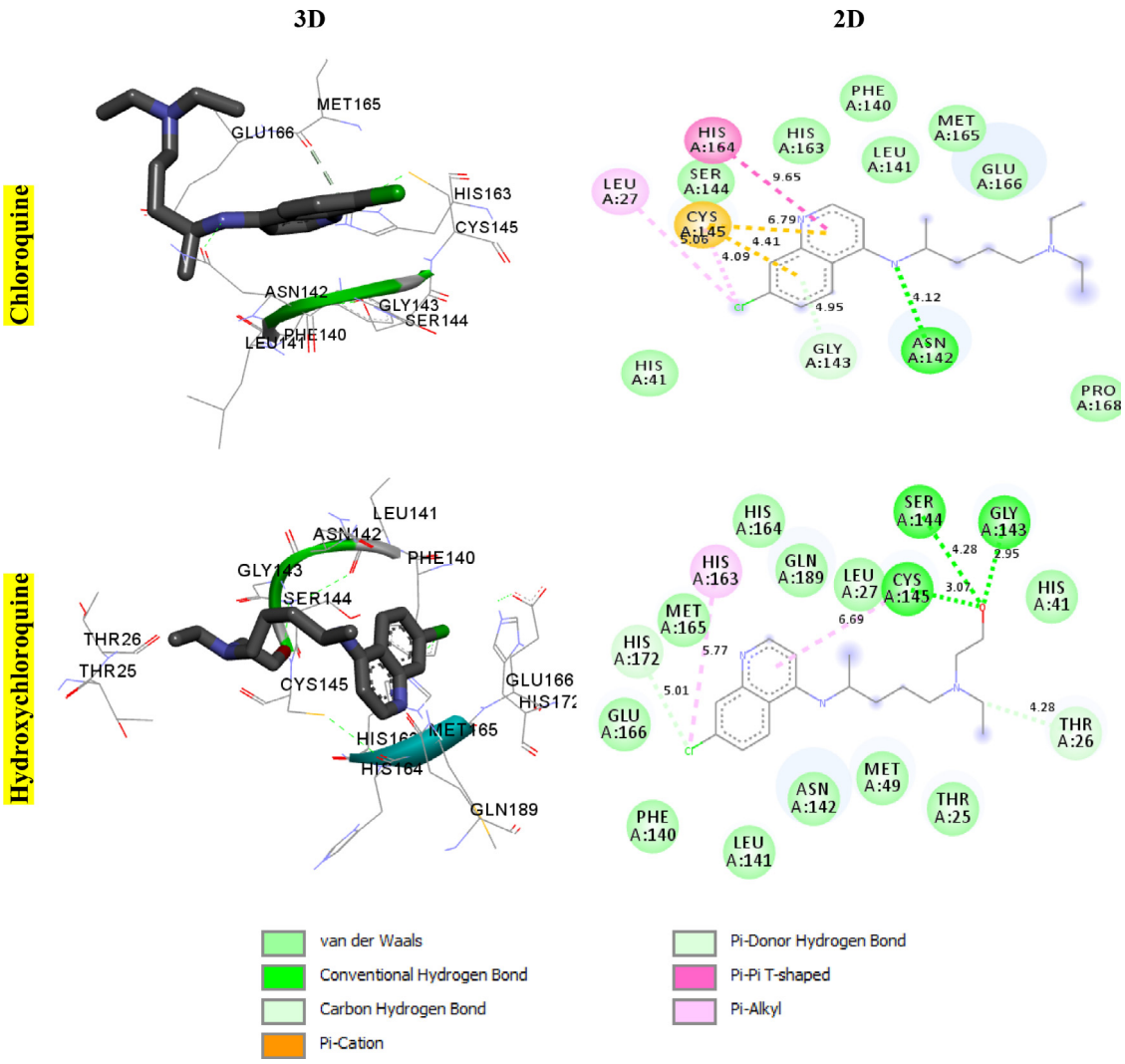


**Fig. 9.** Continued

*3.3.2. Evaluation of the antibacterial activity*

Among the examined strains (Table 6), only *P. aeruginosa* was susceptible to the **HYDZ-1** (15 mm) and **HYDZ-2** (7 mm). Although, *P. aeruginosa* is intrinsically resistant to many antibiotics [72], and is capable of rapidly acquire additional resistance during treatment is a frequent source of therapeutic failure [73], its double membrane structure specific to lipids makes it sensitive to lipophilic substances, which affect the membrane integrity and permeability and would lead to the lysis of the bacterial cell. On the other hand, according to *Haenni* et al. [73], the microbiological studies showed that the presence of an aromatic or a hetero aromatic moiety containing more lipophilic character significantly contributed to antibacterial activity. *El-Etrawy et al.* [74] attributed the inhibitory effect of the new synthesized hydrazones against pathogenic bacteria to its ability to activate enzymes and some cellular proteins essential for ATP synthesis and expression of ribosomal subunit proteins. Studying the structure-activity relationship suggests that different substitutions on aromatic rings affected drastically the antibacterial activity of the synthesized compounds [75]. In the same way, the presence of electronegative atoms and groups (-$NO_2$, -Cl, S-H and N–H) on aromatic rings improves the antimicrobial activity of the compounds [76]. The presence of active functions on the aromatic ring, N=C groups of hydrazones and thiophene motif enhances the antibacterial activity of the studied compounds. This activity remains bacteriostatic and lower than gentamicin. This activity, with 4 mg (20 µl), is satisfying in comparison with other studies [75,77], where high concentrations were used (50 µL, 35 µL). These observations suggest that the molecular targets of **HYDZ-1** and **HYDZ-2** are very different from the other molecules as well as those of conventional antibiotics.

*3.3.3. Evaluation of the ADME-T activity*

Drug-likeness of the synthesized compounds compared with the known drugs was evaluated under Lipinski's rule. In general, an orally active drug fulfill the following criteria: Not more than 5 hydrogen bond donors (n-OH and n-NH), not more than 10 hydrogen bond acceptors (n-ONs), molecular weight (MW) less than 500 D, not more than one violation and octanol-water partition coefficient (milogP) should be not more than 5 [78]. As it can be seen from Table 7, all our hydrazone derivatives did not show any violation of Lipinski's rules with showing a good solubility. Contrarily to the standards, and as an example, chloroquine drugs exhibited one violation, which poses risks of mutagenic and irritation. On the other hand, in the toxicity profile, the studied compounds were ranged as relatively safe species, except standards which showed a risk of toxicity. The tested compounds did not show any risk of toxicity. Consequently, they do not cause any mutagenic, tumorigenic, irritation, or reproductive effect. These results suggest that the synthesized hydrazones have good ADME-T parameters and can be conducive candidates as drugs.

**Table 9**
Molecular docking results interactions and distance of the investigated inhibitors with SARS-CoV-2 main protease.

| Compounds | Amino acid Interactions | Distance (Å) | Type of the interaction |
|---|---|---|---|
| **HYDZ-1** | - LEU141 | 6.35 | Hydrogen bond |
| | - HIS172 | 4.93 | vdW |
| | - MET49, HIS141, MET 165 | 5.44, 5.14, 5.32 | Pi-sulfur |
| | - MET165 | 5.24 | Pi-sigma |
| **HYDZ-2** | - ARG 217, THY 304 | 5.44, 3.83 | Hydrogen bond |
| | - GLN 256 | 4.11 | Pi-sigma |
| | - VAL 303 | 6.24 | vdW |
| **HYDZ-3** | - CYS145, GLY143, | 3.55, 3.41, 3.93, 3.36, 4.57. | Hydrogen bond |
| | SER144,SER 144, HIS163 | 6.00 | Hydrogen bond |
| | - CYS145 | 5.18 | Pi-Alkyl |
| | - GLU166 | 6.08 | vdW |
| | - MET165 | 4.71 | Pi-sigma |
| | - MET 165 | | Pi-cation |
| **Chloroquine*** | - ASN 142 | 4.12 | Hydrogen bond |
| | - HIS 164 | 9.65 | Pi-Pi T-shaped |
| | - LEU 27 CYS 145 | 5.00, 4.09 | Pi-Alkyl |
| | - CYS 145 CYS 145 | 4.41, 6.79 | Pi-cation |
| | - GLY 143 | 4.95 | vdW |
| **Hydroxychloroquine*** | - GLY143, SER 144, CYS | 2.95, 4.28, 3.07 | Hydrogen bond |
| | 145 | 6.69, 5.77 | Pi-Alkyl |
| | - CYS145 HIS163 | 5.01, 4.28 | vdW |
| | - HIS172 THR 26 | | |

* : Drugs Reference.

### 3.4. Molecular docking analysis

The different interactions and their energies between an inhibitor and amino acids inside the active sites of enzymes have been determined by molecular docking simulations. In this context, the energy distribution of different interactions between the Mpro and the synthesized ligands are illustrated in Table 8, which explains the different interactions between the active amino acids of the targeted receptor (Mpro), and **HYDZ-1, HYDZ-2** and **HYDZ-3** [79]. The obtained crystal structures of the best docked modes for Mpro-HYDZ-1, Mpro-HYDZ-2 and Mpro-HYDZ-3 complexes are represented in Fig. 8. It is to be noted that the investigated ligands preferably bind in the external structure of Mpro [38]. Also, the 3D and 2D binding-interaction diagrams of **HYDZ-1, HYDZ-2** and **HYDZ-3** with SARS-CoV-2 main protease are shown in Fig. 9. Generally, the presence of hydrogen bonds is crucial for the interaction between inhibitors and receptors. In this context, the interpretation of the 3D and 2D interaction diagrams indicates the presence of the following types of interactions:

In Table 9, **HYDZ-1** ligand was found to interact with a single conventional hydrogen bond LEU141 (6.35 Å) with the oxygen of the carboxylic group, a Pi-sigma type with MET165 (5.24 Å) and the benzene group, a Pi-Sulfur with MET49 (5.44 Å), HIS41 (5.14 Å) and MET165 (5.32 Å) and thiophene group, a VDW bond with HIS172 (4.93 Å) and carboxylic group.

**HYDZ-2** ligand was also observed to interact through two conventional hydrogen bonds ARG217 (5.44 Å) and THR304 (3.83 Å) with the oxygen of the carboxylic and amine groups of the hydrazone, respectively, a Pi-sigma type with GLN256 (4.11 Å) and a vdW with VAL303 (6.24 Å) with thiophene and C = N function, respectively.

As to **HYDZ-3** ligand, it has interacted through five hydrogen bonds with CYS145 (3.55 Å), GLY143 (3.41 Å), SER144 (3.93 Å), SER144 (3.36 Å) and HIS163 (4.57 Å) which reacted on the carboxylic group, a Pi-Alkyl with CYS145 (6.00 Å), a Pi-Cation with MET165 (4.71 Å) reacted on the furan group, a VDW with GLU166 (5.18 Å) and Pi-Sigma with MET165 (6.08 Å) and benzene group.

For the standard Chloroquine, there is only one hydrogen bonding of ASN142 (4.12 Å) with amine group. Then, a Pi-Alkyl with LEU27 (5.00 Å) and CYS145 (4.09 Å) with the Chlorure atom, a Pi-Cation with CYS145 (4.41 Å), CYS145 (6.79 Å) react on the quinoleine group, a Pi-Pi T-shaped with HIS164 (9.65 Å), GLY143 (4.95 Å) of vdW interaction.

For Hydroxychloroquine, there are three hydrogen bonds of GLY143 (2.95 Å), SER144 (4.28 Å) and CYS145 (3.07 Å) with OH function, two bonds of Pi-Alkyl of CYS145 (6.69 Å), HIS163 (5.77 Å), two van der Waals bonding of HIS172 (5.01 Å), and THR (4.28 Å) interacted with Chlorure atom and amine groups of hydroxychloroquine, respectively.

Pi-Pi Cation, Pi-Sulfur and Pi-alkyl type interactions are included in the hydrophobic category of van der Waals forces, while the hydrophilic interactions included H-bonding forces [38,80]. From these results, we observe that **HYDZ-1, HYDZ-2** and **HYDZ-3** have a Pi-Sigma bond which does not appear in the standards. This means that the inhibitive effect has increased. We can conclude that the amino acids reacted more strongly at the nucliphilic sites (hydroxy, furan and thiophene groups).

Fig. 10 shows the interactions with the molecular surface around the studied ligands at the binding site of Mpro. Accordingly, the green area represents the electron acceptor region, while the pink area represents the electron donor one. The calculated inhibitor-receptor complex interactions showed very positive results [81]. Table 10 gathers comparative values of binding energies of the compounds according to the following order: **HYDZ-1** > **HYDZ-2** > **HYDZ-3** > Chloroquine > Hydroxychloroquine drugs. As a result, the investigated ligands showed a good inhibitory ability against SARS-CoV-2 main protease than standards (Hydroxychloroquine and Chloroquine). Also, **HYDZ-1** ligand showed a better docking score (−89.90 kcal/mol) than other compounds.

**Table 10**
Comparison of the binding energy of HYDZ-1, HYDZ-2 and HYDZ-3 with these of some drugs.

| Compounds | Binding energy in Kcal/mol |
|---|---|
| HYDZ-1 | - 89.90 |
| HYDZ-2 | −85.66 |
| HYDZ-3 | - 84.82 |
| Chloroquine* | - 83.91 |
| Hydroxychloroquine* | - 82.27 |

* : Drugs Reference.

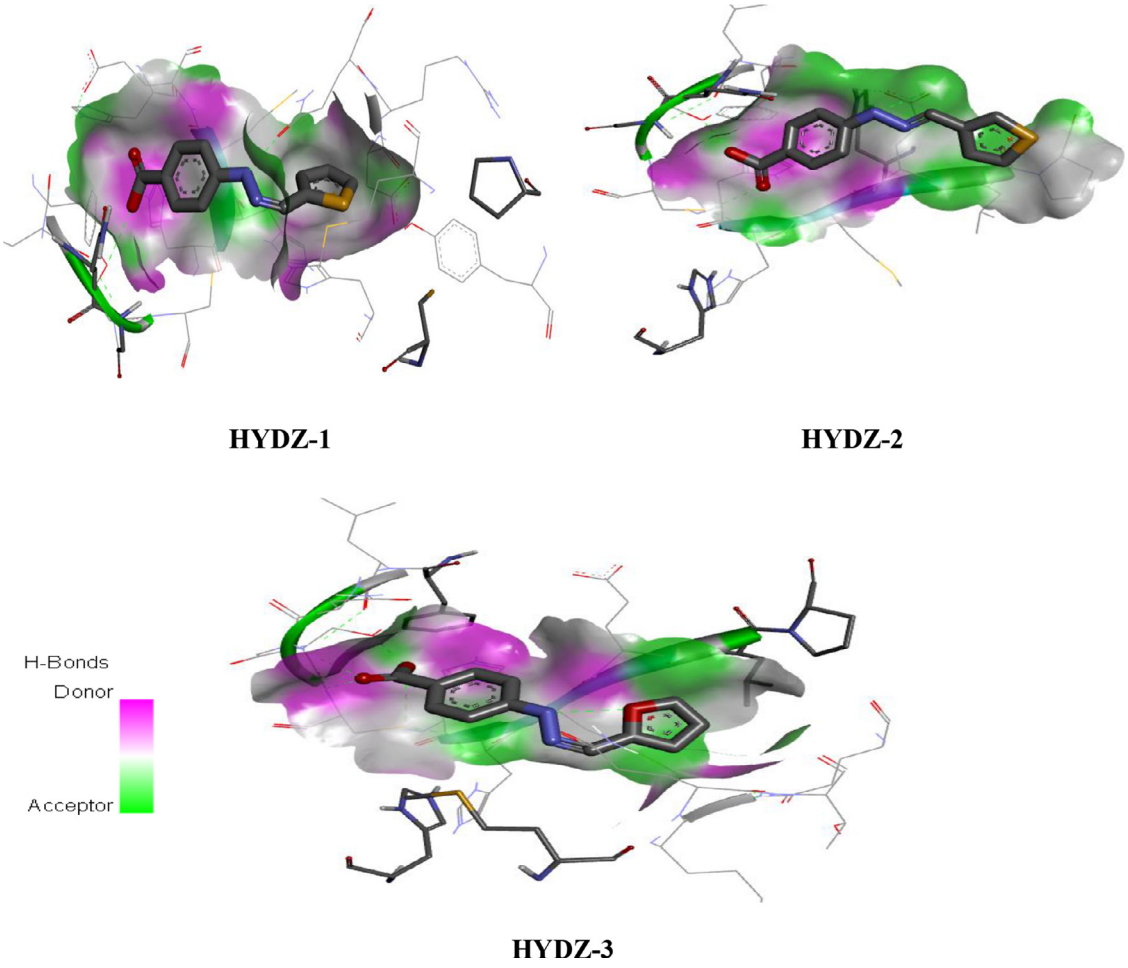


**Fig. 10.** Ligands interaction with their molecular surface maps inside the active site pocket.

## 4. Conclusion

In the present work, we have synthesized three new bioactive hydrazones. The obtained compounds were characterized by high melting points and their structures were determined by UV–Vis, IR, $^{1}$H MNR, $^{13}$C NMR and $^{15}$N NMR. Moreover, the quantum chemical study of the investigated hydrazones has been performed applying DFT method with B3LYP/6–311++*G*(d,p) basis set. IR and UV–Vis theoretical results were found in good agreement with the experimental results. Besides, the calculated values of $E_{HOMO}$ indicated that the investigated **HYDZ-3** is the more electron donor sharing electrons with the acceptor species. Also, the obtained values of $\Delta E_{GAP}$ showed the high reactivity and non-stability of **HYDZ-1**. The calculated MEP illustrated that the electrophilic reaction possible sites are located at the O16, O17, N18 and N19 atoms for **HYDZ-1**, O14, O15, N16 and N17 atoms for **HYDZ-2**, and O14, O15, N16 and N17 atoms for **HYDZ-3**. According to the NBO charge results, oxygen and nitrogen atoms are the most negatively charged. The *in vitro* evaluation of the antioxidant activity of the examined hydrazones demonstrated that **HYDZ-3** shows a higher activity with DPPH than standards, using ABTS assays, while in FRAP and Phenanthroline assays **HYDZ-1** showed a good activity compared to standards. The antibacterial activity was obtained with all three hydrazone derivatives. **HYDZ-1** showed a moderate pseudomonas bacteriostatic activity compared to gentamicin. Also, the predicted ADME-T and pharmacokinetic parameters indicated that these compounds have a good oral bioavailability and show a powerful biological activity. So, the biological study demonstrated that **HYDZ-1** and **HYDZ-3** can be regarded as promising new radical scavengers and oxidative stress inhibitors for the treatment of liver disorders and could be a lead for new, effective, and safe drugs. On the other hand, the calculated binding energies of Mpro-HYDZ-1, Mpro-HYDZ-2 and Mpro-HYDZ-3 complexes indicated the ability of **HYDZ-1** to inhibit SARS-CoV-2 main protease. Finally, the docking results allowed to conclude that the investigated hydrazones derivatives may be developed as therapeutic agents against SARS-CoV-2.

## Declaration of Competing Interest

The authors declare that they have no known competing financial interests or personal relationships that could have appeared to influence the work reported in this paper.

## CRediT authorship contribution statement

**Lilia Adjissi:** Writing – review & editing, Data curation, Formal analysis, Methodology, Resources, Investigation. **Nadjib Chafai:** Conceptualization, Methodology, Validation, Supervision, Project administration, Resources, Investigation, Writing – review & editing. **Khalissa Benbouguerra:** Supervision. **Imene Kirouani:** Writing – review & editing. **Abdelkader Hellal:** Supervision, Writing – review & editing. **Houdheifa Layaida:** Writing – review & editing. **Meriem Elkolli:** Supervision, Writing – review & editing. **Chawki Bensouici:** Supervision, Writing – review & editing. **Salah Chafaa:** Project administration, Supervision, Writing – review & editing.

## Data availability

No data was used for the research described in the article.

## Acknowledgements

This research was supported by the General Directorate for Scientific Research and Technological Development (DGRSDT), Algerian Ministry of Scientific Research, Laboratory of Electrochemistry of Molecular Materials and Complex (LEMMC), Ferhat ABBAS University of Sétif.

## Supplementary materials

Supplementary material associated with this article can be found, in the online version, at doi:10.1016/j.molstruc.2022.134005.

## References

[1] S. Narayanan, P. Gupta, U. Nazim, M. Ali, N. Karadkhelkar, M. Ahmad, Z.S. Hen, Anti-cancer effect of Indanone-based thiazolyl hydrazone derivative on colon cancer cell lines, Int. J. Biochem. Cell Biol. 110 (2019) 21–28.
[2] S. Dasgupta, S. Karim, S. Banerjee, M. Saha, K.D. Saha, D. Das, Designing of novel zinc (II) Schiff base complexes having acyl hydrazone linkage: study of phosphatase and anti-cancer activities, in: Dalton Trans., 49, 2020, pp. 1232–1240.
[3] B. Nikolova-Mladenova, G. Momekov, D. Ivanov, A. Bakalova, Design and drug–like properties of new 5-methoxysalicylaldehyde based hydrazones with anti-breast cancer activity, J. Appl. Biomed. 15 (2017) 233–240.
[4] R.M. Mohareb, J. Schatz, Anti-tumor and anti-leishmanial evaluations of 1,3,4- oxadiazine, pyran derivatives derived from cross-coupling reactions of $\beta$-bromo-6H-1,3,4-oxadiazine derivatives, Bioorg. J. Med. Chem. 19 (2011) 2707–2713.
[5] L. Popiołek, Hydrazide–hydrazones as potential antimicrobial agents: overview of the literature since 2010, Med. Chem. Res. 26 (2017) 287–301.
[6] Ł. Popiołek, Updated Information on Antimicrobial Activity of Hydrazide–Hydrazones, Int. J. Mol. Sci. 22 (2021) 1–20, doi:10.3390/ijms22179389.
[7] T.M. Osório, F.D. Monache, L.D. Chiaradia, A. Mascarello, T.R. Stumpf, C.R. Zanetti, D.B. Silveira, C.R.M. Barardi, E. de Fatima Albino Smânia, A. Viancelli, L.A.T. Garcia, R.A. Yunes, R.J. Nunes, A. Smânia, Antibacterial activity of chalcones, hydrazones and oxadiazoles against methicillin-resistant Staphylococcus aureus, Bioorg. Med. Chem. Lett. 22 (2012) 225–230.
[8] M. Asif, A. Husain, Analgesic, anti-inflammatory and antiplatelet profile of hydrazones containing synthetic molecules, J. Appl. Chem. 2013 (2013) 1–7.
[9] E.N. Nfor, A. Husian, F. Majoumo-Mbe, I.N. Njah, O.E. Offiong, S.A. Bourne, Synthesis, crystal structure and antifungal activity of a Ni (II) complex of a new hydrazone derived from antihypertensive drug hydralazine hydrochloride, Polyhedron 63 (2013) 207–213.
[10] V. Angelova, V. Karabeliov, P.A. Andreeva-Gateva, J. Tchekalarova, Recent developments of hydrazide/hydrazone derivatives and their analogs as anticonvulsant agents in animal models, Drug Dev. Res. 77 (2016) 379–392.
[11] S. Kumar, S. Bawa, S. Drabu, R. Kumar, L. Machawal, Synthesis and *in vivo* anticonvulsant evaluation of 2-chloroquinolinyl hydrazone derivatives, Acta Pol. Pharm. 67 (2010) 567–573.
[12] F.R. Pavan, P.I.D. Maia, S.R.A. Leite, V.M. Deflon, A.A. Batista, D.N. Sato, S.G. Franzblau, C.Q.F. Leite, Thiosemicarbazones, semicarbazones, dithiocarbazates and hydrazide/hydrazones: anti-Mycobacterium tuberculosis activity and cytotoxicity, Eur. J. Med. Chem. 45 (2010) 1898–1905.
[13] M.C. Mandewale, B. Thorat, Y. Nivid, R. Jadhav, A. Nagarsekar, R. Yamgar, Synthesis, structural studies and antituberculosis evaluation of new hydrazone derivatives of quinoline and their Zn(II) complexes, J. Saudi Chem. Soc. 22 (2018) 218–228.
[14] S. Alberca, E. Matador, J. Iglesias-Sigüenza, M. Gracia Retamosa, R. Fernández, J.M. Lassaletta, D. Monge, Asymmetric cross-aldol reactions of $\alpha$-keto hydrazones and $\alpha$, $\beta$-unsaturated $\gamma$-keto hydrazones with trifluoromethyl ketones, Chem. Comm. 57 (2021) 11835–11838.
[15] P. Vicini, M. Incerti, I.A. Doytchinova, P.La Colla, B. Busonera, R. Loddo, Synthesis and antiproliferative activity of benzo[*d*]isothiazole hydrazones, Eur. J. Med. Chem. 41 (2006) 624–632.
[16] S. Sarkar, A.A. Siddiqui, S.J. De, R. Saha, S. Mazumder, C. Banerjee, U. Bandyopadhyay, Antimalarial activity of small-molecule benzothiazole hydrazones, Antimicrob. Agents Chemother. 60 (2016) 4217–4228.
[17] P. Vicini, M. Incerti, P.La Colla, R. Loddo, Anti-HIV evaluation of benzo[*d*]isothiazole hydrazones, Eur. J. Med. Chem. 44 (2009) 1801–1807.
[18] M. Karnatak, M. Hassam, A.S. Singh, D.K. Yadav, C. Singh, S.K. Puri, P.V. Verma, Novel hydrazone derivatives of N-amino-11-azaartemisinin with high order of antimalarial activity against multidrug-resistant Plasmodium yoelii nigeriensis in Swiss mice via intramuscular route, Bioorganic Med. Chem. Lett 58 (2022) 128522.
[19] A.B. Thomas, R.K. Nanda, L.P. Kothapalli, S.C. Hamane, Synthesis and biological evaluation of Schiff's bases and 2-azetidinones of isonocotinylhydrazone as potential antidepressant and nootropic agents, Arab. J. Chem 9 (2016) S79–S90.
[20] A. Baier, A. Kokel, W. Horton, E. Gizińska, G. Pandey, R. Szyszka, B. Török, M. Török, Organofluorine hydrazone derivatives as multifunctional anti-Alzheimer's agents with CK2 inhibitory and antioxidant features, Chem. Med. Chem. 16 (2021) 1927–1932.
[21] S. Parlara, G. Sayara, A. Tarikogullaria, Synthesis, bioactivity and molecular modeling studies on potential anti-Alzheimer piperidine hydrazide-hydrazones, Bioorg. Chem 87 (2019) 888–900.
[22] R.A. Hauser-Davis, L.V. de Freitas, D.S. Cukierman, W.S. Cruz, M.C. Miotto, J. Landeira-Fernandez, A.A. Valiente-Gabioud, C.O. Fernandez, N.A. Rey, Disruption of zinc and copper interactions with A beta(1-40) by a non-toxic, isoniazid-derived, hydrazone: a novel biometal homeostasis restoring agent in Alzheimer's disease therapy, Metallomics 7 (2015) 743–747.
[23] K. Benbouguerra, S. Chafaa, N. Chafai, M. Mehri, O. Moumeni, A. Hellal, Synthesis, spectroscopic characterization and a comparative study of the corrosion inhibitive efficiency of an $\alpha$-aminophosphonate and Schiff base derivatives: experimental and theoretical investigations, J. Mol. Struct. 1157 (2018) 165–176.
[24] O. Mohammad, A. Khamaysa, I. Selatnia, Hydrazone-based green corrosion inhibitors for API grade carbon steel in HCl: insights from electrochemical, XPS, and computational studies, Colloids Surf. A 626 (2021) 127047.
[25] N. Chafai, S. Chafaa, K. Benbouguerra, A. Hellal, M. Mehri, Synthesis, spectral analysis, anti-corrosive activity and theoretical study of an aromatic hydrazone derivative, J. Mol. Struct. 1181 (2019) 83–92.
[26] K.B. Gudasi, R.S. Vadavi, R.V. Shenoy, S.A. Patil, M. Nethaji, Crystal Structure of 2-thiophene-2-yl-3(thiophene-2-carboxylideneamino)-1,2-dihydroquinazolin-4(3H)-one and the synthesis, spectral and thermal studies of its transition metal (II) complexes, Transit. Met. Chem. 31 (2006) 374–381.
[27] K.B. Gudasi, R.S. Vadavi, R.V. Shenoy, S.A. Patil, M. Nethaji, Crystal Structure of 2-pyridine-2-yl-3(pyridine-2-carboxylideneamino)quinazolin-4(3H)-one and its ligating diversity towards transition metal (II) ions, Transit. Met. Chem. 31 (2006) 135–145.
[28] J. Pisk, I. Đilović, T. Hrenar, D. Cvijanović, G. Pavlović, V. Vrdoljak, Effective methods for the synthesis of hydrazones, quinazolines, and Schiff bases: reaction monitoring using a chemometric approach, RSC Adv. 10 (2020) 38566–38577.
[29] S. Rollas, Ş.G. Küçükgüzel, Biological activities of hydrazone derivatives, J. Mol. 12 (2007) 1910–1939.
[30] N. Houas, S. Chafaa, N. Chafai, S. Ghedjati, M. Djenane, S. Kitouni, Synthesis, characterization, DFT study and antioxidant activity of (2-hydroxynaphthalen-1-yl)methyl 2-hydroxyphenyl aminophosphonic acid, J. Mol. Struct. 1247 (2022) 131322.
[31] S. Mammeri, N. Chafai, H. Harkat, R. Kerkour, S. Chafaa, Protection of steel against corrosion in acid medium using dihydropyrimidinone derivatives: experimental and DFT study, Iranian J. Sci. Tech, Trans. A 45 (2021) 1607–1619.
[32] M. Djenane, S. Chafaa, N. Chafai, R. Kerkour, A. Hellal, Synthesis, spectral properties and corrosion inhibition efficiency of new ethylhydrogen[(*methoxyphenyl*)(*methylamino*) *methyl*]phosphonate derivatives: experimental and theoretical investigation, J. Mol. Struct. 1175 (2019) 398–413.
[33] N. Chafai, S. Chafaa, K. Benbouguerra, D. Daoud, A. Hellal, M. Mehri, Synthesis, characterization and the inhibition activity of a new $\alpha$-aminophosphonic derivative on the corrosion of XC48 carbon steel in 0.5M $H_2SO_4$ : experimental and theoretical studies, J. Taiwan Inst. Chem. Eng. 70 (2017) 331–344.
[34] S. Zaout, S. Chafaa, A. Hellal, O. Boukhemis, L. Khattabi, H. Merazig, N. Chafai, C. Bensouici, L. Bendjeddou, Hydroxyphenylamine phosphonate derivatives: synthesis, X-ray crystallographic analysis, and evaluation of theirs anti-Alzheimer effects and antioxidant activities, J. Mol. Struct. 1225 (2021) 129121.
[35] N. Chafai, K. Benbouguerra, S. Chafaa, A. Hellal, Quantum chemical study of Hydroxychloroquine and Chloroquine drugs used as a treatment of COVID-19, Iran. J. Chem. Chem. Eng. 41 (2022) 27–36.
[36] A. Hellal, R. Djebaili, S. Zaout, M. Elkolli, S. Chafaa, L. Touafri, N. Chafai, M. Mehri, K. Benbougerra, Structural, electronic, vibrational, optical and thermodynamic properties of 3-Oxo-3-p-tolylpropylphosphonic acid and 4-Oxo-4-p-tolyl-butyric acid: density functional theory study, J. Mol. Struct. 117 (2018) 527–540.
[37] A. Hellal, S. Chafaa, N. Chafai, Synthesis, characterization and computational studies of three $\alpha$-aminophosphonic acids derivatives from Meta, Ortho and Para aminophenol, J . Mol. Struct. 1103 (2016) 110–124.
[38] K. Benbouguerra, N. Chafai, S. Chafaa, Y.I. Touahria, H. Tlidjane, New $\alpha$-Hydrazinophosphonic acid: synthesis, characterization, DFT study and in silico prediction of its potential inhibition of SARS-CoV-2 main protease, J. Mol. Struct. 1239 (2021) 130480.
[39] M.A. Said, D.J. Khan, F.F. Al-blewi, N.S. Al-Kaff, A.A. Ali, N. Rezki, M. Hagar, New 1,2,3-triazole scaffold schiff bases as potential anti-covid-19: design, synthesis, DFT-molecular docking, and cytotoxicity aspects, Vaccines (Basel) 9 (2021) 1012.
[40] S. Abu-Melha, M.M. Edrees, S.M. Riyadh, M.R. Abdelaziz, A.A. Elfiky, S.M. Gomha, Clean grinding technique: a facile synthesis and *in silico* antiviral activity of hydrazones, pyrazoles, and pyrazines bearing thiazole moiety against SARS-CoV-2 main protease (Mpro), Molecules 25 (2020) 1–13.
[41] N. Hosny, Y. Sherif, Molecular docking study on some isonicotinoyl hydrazide derivatives as potential inhibitors of COVID-19, Letters Appl. Nano Bio Sci. 3 (2020) 1217–1224.
[42] H. Boulebd, Y. Zine, I.A. Khodja, A. Mermer, A. Demir, A. Debache, Synthesis and radical scavenging activity of new phenolic hydrazone/hydrazide derivatives: experimental and theoretical studies, J. Mol. Struct. 1249 (2022) 131546.

[43] A. Hellal, S. Chafaa, N. Chafai, L. Touafri, Synthesis, antibacterial screening and DFT studies of series of $\alpha$-aminophosphonates derivatives from aminophenols, J. Mol. Struct. 1134 (2017) 217–225.
[44] W. Kohn, L.J. Sham, Quantum density oscillations in an inhomogeneous electron gas, Phys. Rev. A 137 (1965) 1697–1705.
[45] M. Arivazhagan, V.P. Subhasini, Quantum chemical studies on structure of 2-amino-5-nitropyrimidine, Spectrochim. Acta, Part A 91 (2012) 402–410.
[46] M.S. Blois, Antioxidant determinations by the use of a stable free radical, NatureNature 181 (1958) 1199–1200.
[47] R. Re, N. Pellegrini, A. Proteggente, A. Pannala, M. Yang, C. Rice-Evans, Antioxidant activity applying an improved ABTS radical cation decolorization assay, Free Radical Bio. Med. 26 (1999) 1231–1237.
[48] R. Apak, K. Güçlü, M. Ozyürek, S.E. Karademir, Novel total antioxidant capacity index for dietary polyphenols and vitamins C and E, using their cupric ion reducing capability in the presence of Neocuproine: CUPRAC method, J. Agric. Food Chem. 52 (2004) 7970–7981.
[49] M. Oyaizu, Studies on products of browning reactions. Antioxidative activities of browning reaction prepared from glucosamine, Jpn. J. Nutr. Diet 44 (1986) 307–315, doi:10.5264/eiyogakuzashi.44.307.
[50] A. Szydlowska-Czerniaka, C. Dianoczki, K. Recseg, G. Karlovits, E. Szlyk, Determination of antioxidant capacities of vegetable oils by ferric-ion spectrophotometric methods, TalantaTalanta 76 (2008) 899–905.
[51] A.W. Bauer, Antibiotic susceptibility testing by a standardized single disc method, Am. J. Clin. Pathol. 45 (1966) 149–158.
[52] M. El Kolli, H. Laouer, H. El Kolli, S. Akkal, F. Sahli, Chemical analysis, antimicrobial and anti-oxidative properties of Daucus gracilis essential oil and its mechanism of action, Asian Pac J Trop Biomed 6 (2016) 8–15.
[53] I.A. Khodja, H. Boulebd, C. Bensouici, A. Belfaitah, Design, synthesis, biological evaluation, molecular docking, DFT calculations and in silico ADME analysis of (benz) imidazole-hydrazone derivatives as promising antioxidant, antifungal, and anti-acetylcholinesterase agents, J. Mol. Struct. 1218 (2020) 128527.
[54] P. Chowdhury, P. Pathak, Neuroprotective immunity by essential nutrient “Choline” for the prevention of SARS CoV2 infections: an in silico study by molecular dynamics approach, Chem. Phys. Lett. 761 (2020) 138057, doi:10.1016/j.cplett.2020.138057.
[55] E. Yuriev, M. Agostino, P.A. Ramsland, Challenges and advances in computational docking: 2009 in review, J. Mol. Recognit. 24 (2011) 149–164.
[56] C.P. Gros, A. Eggenspiller, A. Nonat, J.M. Barbe, F. Denat, New potential bimodal imaging contrast agents based on DOTA-like and porphyrin macrocycles, Med. Chem. Commun 2 (2011) 119–125, doi:10.1039/C0MD00205D.
[57] P.M. Jeffrey, M. Damian, R. Leo, An evaluation of harmonic vibrational frequency scale factors, J. Phys. Chem. 111 (2007) 11683–11700.
[58] M. Mehri, N. Chafai, L. Ouksel, K. Benbouguerra, A. Hellal, S. Chafaa, Synthesis, electrochemical and classical evaluation of the antioxidant activity of three $\alpha$-aminophosphonic acids: experimental and theoretical, J. Mol. Struct. 1171 (2018) 179–189.
[59] O. Moumeni, S. Chafaa, R. Kerkour, K. Benbouguerra, N. Chafai, Synthesis, structural and anticorrosion properties of diethyl(phenylamino)methyl)phosphonate derivatives: experimental and theoretical study, J. Mol. Struct. 1206 (2020) 127693.
[60] R. Kerkour, S. Chafaa, N. Maouche, O. Moumeni, N. Chafai, Corrosion inhibition of stainless steel N304 by dihydroxy benzyl phosphonic acid in 0.5M $H_2SO_4$ : experimental and theoretical studies, Indian J. Chem. Technol. 26 (2019) 69–75.
[61] L. Herrag, B. Hammouti, S. Elkadiri, A. Aouniti, C. Jama, H. Vezin, F. Bentiss, Adsorption properties and inhibition of mild steel corrosion in hydrochloric solution by some newly synthesized diamine derivatives: experimental and theoretical investigations, Corros. Sci. 52 (2010) 3042–3051.
[62] K.F. Khaled, Studies of iron corrosion inhibition using chemical, electrochemical and computer simulation techniques, Electrochim. Acta 55 (2010) 6523–6532.
[63] H.A. Arjun, G.N. Anil Kumar, R. Elancheran, S. Kabilan, Crystal structure, DFT and Hirshfeld surface analysis of (E)-N′-[(1-chloro-3, 4-dihydronaphthalen-2-yl) methylidene] benzohydrazide monohydrate, Acta Crystallogr. Section E 76 (2020) 132–136.
[64] U. Vanitha, R. Elancheran, V. Manikandan, S. Kabilan, K. Krishnasamy, Design, synthesis, characterization, molecular docking and computational studies of 3-phenyl-2-thioxoimidazolidin-4-one derivatives, J. Mol. Struct. 1246 (2021) 131212.
[65] A. Stoyanova, G. Petkova, S.D. Peyerimhoff, Correlation between the molecular structure and the corrosion inhibiting effect of some pyrophthalone compounds, Chem. Phys. 279 (2002) 1–6.
[66] T.K. Chaitra, K.N. Mohana, D.M. Gurudatt, H.C. Tandon, Inhibition activity of new thiazolehydrazones towards mild steel corrosion in acid media by thermodynamic, electrochemical and quantum chemical methods, J. Taiwan Inst. Chem. Eng. 67 (2016) 521–531.
[67] M. Rafiq, M. Khalid, M.N. Tahir, M.U. Ahmad, M.U. Khan, M.M. Naseer, A.A.C. Braga, S. Muhammad, Z. Shafiq, Synthesis, XRD, spectral (IR, UV–Vis, NMR) characterization and quantum chemical exploration of benzoimidazole-based hydrazones: a synergistic experimental-computational analysis, J. Appl. Organomet. Chem. 33 (2019) 1–17.
[68] T. Yesilkaynak, G. Binzet, F.M. Emen, U. Flörke, N. Külcü, Theoretical and experimental studies on N-(6-methylpyridin-2-yl-carbamothioyl)biphenyl-4-carboxamide, Eur. J. Chem. 1 (2010) 1–5.
[69] H. Kargar, M. Fallah-Mehrjardi, R. Behjatmanesh-Ardakani, K.S. Munawar, M. Ashfaq, M.N. Tahir, Diverse coordination of isoniazid hydrazone Schiff base ligand towards iron (III): synthesis, characterization, SC-XRD, HSA, QTAIM, MEP, NCI, NBO and DFT study, J. Mol. Struct. 1250 (2022) 131691.
[70] R. Elancheran, K. Saravanan, S. Divakar, S. Kumari, V.L. Maruthanila, S. Kabilan, M. Ramanathan, R. Devi, J. Kotoky, Design, synthesis and biological evaluation of novel 1, 3-thiazolidine-2, 4-diones as anti-prostate cancer agents, Anticancer Agents Med. Chem. 17 (2017) 1756–1768.
[71] S.Y. Çiftci, N.G. Kelekçi, U.S. Gökşen, G. Uçar, Free-radical scavenging activities of 2-benzoxazolinone derivatives containing thiosemicarbazide, triazole, thiadiazole and hydrazone units, Hacettepe Univ. J. Faculty Pharmacy 31 (2011) 27–50.
[72] A. Lupo, M. Haenni, J.Y. Madec, Antimicrobial resistance in acinetobacter spp. and pseudomonas spp, Microbiol. Spectr. 6 (2018) 1–16.
[73] M. Haenni, D. Hocquet, C. Ponsin, P. Cholley, C. Guyeux, J.Y. Madec, X. Bertrand, Population structure and antimicrobial susceptibility of Pseudomonas aeruginosa from animal infections in France, BMC Vet. Res. 11 (2015) 1–5.
[74] A.A.S. El-Etrawy, F.F. Sherbiny, Design, synthesis, biological evaluation and molecular modeling investigation of new N'-(2-Thiouracil-5-oyl) hydrazone derivatives as potential anti-breast cancer and anti-bacterial agents, J. Mol. Struct. 1232 (2021) 129993.
[75] W. Gu, R. Wu, S. Qi, C. Gu, F. Si, Z. Chen, Synthesis and antibacterial evaluation of new *N*-acylhydrazone derivatives from dehydroabietic acid, Molecules 17 (2012) 4634–4650.
[76] A. Deep, S. Jain, P.C. Sharma, P. Verma, M. Kumar, C.P. Dora, Design and biological evaluation of biphenyl-4-carboxylic acid hydrazide-hydrazone for antimicrobial activity, Act Pol. Pharm. 67 (2010) 255–259.
[77] N. Özbek, Ü.Ö. Özdemir, A.F. Altun, E. Şahin, Sulfonamide-derived hydrazone compounds and their Pd (II) complexes: synthesis, spectroscopic characterization, X-ray structure determination, *in vitro* antibacterial activity and computational studies, J. Mol. Struct. 1196 (2019) 707–719.
[78] C.A. Lipinski, F. Lombardo, B.W. Dominy, P.J. Feeney, Experimental and computational approaches to estimate solubility and permeability in drug discovery and development settings, Adv. Drug Deliv. Rev. 23 (1997) 3–25.
[79] S. Gatfaoui, A. Sagaama, N. Issaoui, T. Roisnel, H. Marouani, Synthesis, experimental, theoretical study and molecular docking of 1-ethylpiperazine-1,4-diiumbis(nitrate), Solid State Sci. 106 (2020) 106326.
[80] T. Topal, Y. Zorlu, N. Karapınar, Synthesis, X-ray crystal structure, IR and Raman spectroscopic analysis, quantum chemical computational and molecular docking studies on hydrazone-pyridine compound: as an insight into the inhibitor capacity of main protease of SARS-CoV-2, J. Mol. Struct. 1239 (2021) 130514.
[81] M. Venkateshan, M. Muthu, J. Suresh, R.R. Kumar, Azafluorene derivatives as inhibitors of SARS-CoV-2 RdRp: synthesis, physicochemical, quantum chemical, modeling and molecular docking analysis, J. Mol. Struct. 1220 (2020) 128741.